Guidelines and recommendations for ship design on bubble sweep down avoidance

15 November 2016 – Version 1.4

Grant Agreement n° 312762

Acronym: EUROFLEETS2

Title: New operational steps towards an alliance of European research fleets

Activity type: JRA
WP N°: 11 Regional RVs guidelines and generic designs
Task N°: 11.2.2 Bubble sweep down avoidance
Deliverable N°: D11.3

Reference : EUROFLEETS2-WP11-D11.3-151116-V1.4
Security : Public

Document information	
Document Name	Guidelines and recommendations for ship design on bubble sweep down avoidance
Document ID	EUROFLEETS2-WP11-D11.3-151116-V1.4
Revision	1.4
Revision Date	15/11/16
Author	C. Leotardi, E.F. Campana (CNR)
Security	Public

Approvals				
	Name	**Organisation**	**Date**	**Visa**
Coordinator	Valerie Mazauric	IFREMER		
Activity Coordinator	Serge Scory	RBINS		
WP Leaders	Emilio Fortunato Campana	CNR		

History			
Revision	**Date**	**Modification**	**Author**
1	02/11/2015	First release	C.Leotardi and E.F. Campana
2	18/01/2016	Second release	C.Leotardi and E.F. Campana
3	25/06/2016	Third release	C.Leotardi et al.
4	15/11/2016	Forth release	C.Leotardi et al.

Diffusion list				

Contents

1. General context

During the last years oceanography experienced a fast growth eased by recent technological advances in several connected fields. The effectiveness and efficiency of modern research vessels (RVs), such as maximum operative range, endurance, environmentally friendly performances, as well as detection performances have been enhanced taking advantage of the improved reliability and compactness of on board systems (stemming from hybrid and/or fully electric propulsion systems, real-time and remote accessible on-board monitoring systems and high range/bandwidth transmission data devices). Moreover, modern and efficient RVs - designed to be multipurpose - are equipped with high-resolution and sophisticated instruments, which introduced significant challenges for oceanographic ship hull designers. One of the most critical issue is the installation of the sonar systems, i.e. finding the optimal location, configuration, and the optimal hull shape allowing for taking advantage of their full performance, mitigating and/or avoiding the detrimental effects due to bubble sweep-down phenomenon. In fact, whether during survey operations significant bubble sweep-down occurs, it may induce disturbances, such as noise and/or false spots, to the measurements' devices and lead to inaccurate readings, thus forcing the vessel to repeat survey tracks when weather conditions improve, causing extra costs and schedule over-runs.

The bubble sweep-down effect on scientific detecting systems is a widely known phenomenon, somehow experienced on nearly every research vessel. At the very beginning, ex-post researches on this topic were the result of the poor quality sonar performances experienced after the ship deployment. This induced to an *ex post* investigation of technological solutions sought to improve the detection performances. Devices located upstream of the transducers arrays (e.g. fence-like appendages) have been used to force the "bubbling flow" far away the sonar position. Furthermore, several types of appendages and corresponding installations (e.g. wings, gondolas, etc.) have been used to host the transducers, in order to keep them located out the bubble sweep-down region. Such countermeasures, though allowing for a mitigation of the undesirable effect of the bubbles, induce unavoidable effects, such as the drag increase, and eventually the appendage cavitation occurrence. The former effect affects the performance of the RVs, resulting in an increase in fuel consumption (which represent a severe drawback both for environmental and economical viewpoint) and the latter – representing an extra source of noise – might, once more, directly affect the transducers performances and/or might jeopardize other design efforts related to noise and vibration mitigation. Due to this, more recently, modern design paradigms of RVs address also the bubble sweep-down mitigation since the early stage of the process.

In order to take into account the bubble sweep-down phenomenon during the design process its originating mechanism has been investigated and its subsequently briefly recalled. Bubbles originate on the ocean surface and their characteristics (size, density, etc.) strongly depend on the environmental conditions (e.g. wind, sea state conditions, etc.). Moreover, surface vessels - while operating - generate extra bubbles due to the flow evolution in the bow region, since, for example air is entrained during ship motions, wave breaking and thruster emergence. Part of those bubbles, along with the others already formed due to other mechanisms, are entrapped by the flow evolving nearby the hull and are driven both along and under the vessel, mostly following the flow streamlines. As these bubbles flow aft, they might intercept the area where the hydroacoustic transducers are mounted, generating "clouds" or "sheet-like" regions sweeping down and under the vessels. The transducers effectiveness is hence pauperized and a source of undesired broadband noise is generated. Ship motions, especially heave and pitch, can aggravate the bubble phenomenon, affecting size, quantity and the path of the bubbles.

Ship pitching, actually, tends to strengthen the bubble generation and an increased pitch angle can force the streamlines closer to the ship's centerline where the hydroacoustic transducers are usually located. Several studies, also including underwater videos, have documented the dependence of bubble formation on the magnitude of ship pitching, and thus the dependence on sea state and the ship heading relative to the sea state. Moreover, flow around a conventional bow bulb can also cause bubble formation and the generation of a vortex as the water spills in and over the bow bulb during a bow down pitching motion. The vortex leads the bubbles downward and those close to the hull are entrapped into the flow.

Due to the complexity of the phenomenon under investigation, several design paradigms, have been developed in the recent past in order to include as much as the past experience in minimizing the bubble sweep-down from the very beginning of the design process. Efforts focusing on the minimization of the bubble sweep-down through hull design have mostly concentrated on minimizing the effects of air bubbles that originate near the bow and close to the water surface. These efforts require the determination of the streamlines that drive the bubbles downstream, in order to obtain an optimal hull shape that directs the streamlines as far away from acoustic sensors as possible.

The object of this report is to provide guidelines and recommendations on bubble-sweep down avoidance for regional research vessels (RRVs).
Nevertheless, it should be underlined that drawing up guidelines is not easy since it is impossible to determine a "standard" regional vessel and the issue addressed is strongly dependent on the vessel characteristics (essentially hulls' shape as well as inertia distribution). Therefore, the indications for design solutions in order to mitigate the bubble sweep-down phenomenon are given on the basis of the simulation-based design analyses and optimization performed on two vessels' hull shapes and literature knowledge.

2. Mitigation of the bubbles occurrence effects via shape design optimization: the approach

Within this context, a dedicated optimization scheme - whose key points can be summarized as identify the most relevant objective function/s to be minimized/maximized in order to achieve meaningful results in terms of bubble sweep mitigation – has been developed. Specifically, two objective functions are addressed - representing the two most significant phenomena to be evaluated - and are computed varying the hull shapes, taking into account diverse environmental and operating conditions.

The problem has been addressed using a multilevel optimization approach.

2.1 Multilevel optimization

The multilevel optimization approach used for this work includes:

1) a preliminary analysis on the baseline configurations in order to provide for the characterization of the bubble sweep down phenomenon, the corresponding influence parameters, and to define modifications of the hull and/or bulb shapes leading to mitigation of the effects due to bubbles occurrence;
2) a first optimization level, achieved by a single-objective optimization;
3) a second optimization level, achieved by a multi-objective optimization.

Two base hull forms have been identified as representative of the two design concepts, with and without bulb. Two environmental conditions (i.e. sea-state 2 and 6) - indicated as more representative for the purpose of the work - and design/operating speed conditions have been considered.

Optimization level 1:

Two single-objective optimizations are performed. The following objective functions are addressed (one for each optimization):

1) the mean downwards velocity component of the flow (F1), which is correlated to the average angle of streamlines, is evaluated in a prescribed region of the hull for assigned environmental (sea-state) and operating (speed) conditions;
2) the root mean square (RMS) of the bow vertical acceleration (F2) is evaluated in a prescribed point for assigned environmental (sea-state) and operating condition (speed).

Optimization level 2:

The second optimization planned pertains, instead, a multi-objective optimization, considering together both F1 and F2.

2.2 Simulation-based design optimization procedure

The general global optimization problem is defined as

$$\begin{aligned} \text{minimize} \quad & f(\mathbf{x}) \quad && \mathbf{x} \in D \\ \text{subject to} \quad & h_m(\mathbf{x}) = 0 && m = 1, ..., M \\ \text{and to} \quad & g_n(\mathbf{x}) \leq 0 && n = 1, ..., N \end{aligned}$$

where

- f is the objective of optimization task (for the single-objective optimizations f=F1 and f=F2; for the multi-objective optimization f=f(F1,F2));
- h_m represents the *m*-th equality constraint;
- g_n is the *n*-th inequality constraint;
- x is the vector collecting design variables.

In order to solve the problem described above, the following three interconnected elements are essential:

1) tools for computational fluid dynamics (CFD) analyses;
2) tool for geometry modifications;
3) optimization algorithm.

The simulation-based design optimization framework (SBDO) used for the current analysis integrates solvers for calm-water analysis and seakeeping prediction, a design modification method based on linear expansion of orthogonal basis function, and single/multi-objective optimization algorithm based on the particle swarm metaheuristic, which are described in the following.

2.2.1 Tools for CFD analysis

WARP. The WAve Resistance Program is a linear potential flow code, in-house developed at INSEAN. The Neumann-Kelvin linearization is used for the current optimization study. Details of equations, numerical implementations and validation of the numerical solver are given in Bassanini et al. (1994). For optimization purposes, the wave resistance is evaluated by the transverse wave cut method (Telste and Reed, 1994), whereas the frictional resistance is estimated using a flat-plate approximation, based on the local Reynolds number (Schlichting and Gersten, 2000). The steady 2DoFs (sinkage and trim) equilibrium is achieved by iteration of the flow solver and the body equation of motion.

SMP. The Standard Ship Motion program was developed at the David Taylor Naval Ship Research and Development Center in 1981, as a prediction tool for use in the Navy's ship design process. SMP provides a potential flow solution based on linearized strip theory. The 6 DOF response of the ship is given, advancing at constant forward speed with arbitrary heading in both regular waves and irregular seas, as well as the longitudinal, lateral, and vertical responses at specified locations of the ship (Meyers and Baitis, 1981).

WARP and SMP are used to evaluate F1 and F2, respectively.

2.2.2 Tools for geometry modifications

Shape modifications $\boldsymbol{\delta}_s$ are produced by superposition of orthogonal basis functions $\boldsymbol{\psi}_j$, and controlled by N_{DV} design variables α_j, as

$$\boldsymbol{\delta}_s(\xi,\eta) = \sum_{j=1}^{N_{DV}} \alpha_j \boldsymbol{\psi}_j(\xi,\eta) \tag{1}$$

with

$$\boldsymbol{\psi}_j(\xi,\eta) := \sin\left(\frac{p_j\pi\xi}{A_j - B_j} + \phi_j\right)\sin\left(\frac{q_j\pi\eta}{C_j - D_j} + \chi_j\right)\boldsymbol{e}_{k(j)}, \quad (\xi,\eta) \in [A_j; B_j] \times [C_j; D_j] \tag{2}$$

where (ξ,η) are curvilinear coordinates; p_j and q_j respectively define the order of the function in ξ and η direction, φ_j and χ_j are the corresponding spatial phases; A_j, B_j, C_j and D_j define the patch size and $\boldsymbol{e}_{k(j)}$ is a unit vector.

Modifications may be applied in x, y, or z direction, by setting k(j) = 1, 2 or 3, respectively (Campana et al., 2015). Once the shape modification is produced over the selected surface-body patches, the automatic scaling satisfies geometrical equality constraints.

2.2.3 Optimization algorithm

Particle Swarm Optimization (PSO) belongs to the class of heuristic algorithms for single-objective evolutionary derivative-free global optimization and was originally introduced by Kennedy and Eberhart (1995). In order to make PSO more efficient for simulation-based design optimization, a deterministic version of the algorithm (DPSO) has been formulated by Campana et al. (2009), as follows

$$\begin{cases} \mathbf{v}_j^i &= \chi[\mathbf{v}_j^{i-1} + c_1(\mathbf{x}_{j,pb} - \mathbf{x}_j^{i-1}) + c_2(\mathbf{x}_{gb} - \mathbf{x}_j^{i-1})] \\ \mathbf{x}_j^i &= \mathbf{x}_j^{i-1} + \mathbf{v}_j^i \end{cases}$$

that represents velocity and position, respectively, of the *j*-th particle at the *i*-th iteration. Particles are attracted by the personal best position $\mathbf{x}_{i,pb}$ ever found by the *j*-th particle, and by the global best position $\mathbf{x}_{gb}$ ever found by all particles. The effectiveness of DPSO depends on the constriction factor χ, the social and cognitive learning rate c_1 and c_2, along with the number of individuals N_p and their initial distribution and velocity. Serani et al. (2016) investigated the effect of such parameters and proposed guidelines for an efficient use of the algorithm, in the context of ship hydrodynamic optimization. The advantage of using a deterministic version of the algorithm is that a statistical analysis of the results is not necessary (see, e.g., Chen et al., 2015).

The extension of DPSO to multi-objective problems (MODPSO) can be found in Pellegrini et al. (2016). This is based on extending the definition of the personal and global best in the Pareto-optimality sense, and it is formulated as follows

$$\begin{cases} \mathbf{v}_j^i &= \chi[\mathbf{v}_j^{i-1} + c_1(\mathbf{x}_{j,pb} - \mathbf{x}_j^{i-1}) + c_2(\mathbf{x}_{j,gb} - \mathbf{x}_j^{i-1})] \\ \mathbf{x}_j^i &= \mathbf{x}_j^{i-1} + \mathbf{v}_j^i \end{cases}$$

Specifically, $\mathbf{x}_{i,pb}$ is the closest point to $\mathbf{x}_i^{i-1}$ of the personal (cognitive) Pareto front, whereas $\mathbf{x}_{i,gb}$ is the closest point to $\mathbf{x}_i^{i-1}$ of the global (social) Pareto front. The setup suggested by Pellegrini et al. (2016) is used for the multi-objective optimizations. Specifically, N_p is set equal to 16 times the number of design variables. The initialization of the particle swarm is based on a Hammersley sequence sampling (Wong et al., 1997) over

variable domain and bounds, with non-null velocity (Chen et al., 2015). The set of coefficients is taken from Trelea (2003): χ=0.6 and c_1=c_2=1.7. A semi-elastic wall-type approach is used for box constraints (Serani et al., 2016).

During the optimization process inequality constraints are treated by a constant penalty function (the shape modification tool automatically satisfies geometrical equality constraints). The maximum number of function evaluations is set equal to 256 times the number of design variables.

3. Hull with bulb

The original hull with bulb selected to derive indications on the proper design to mitigate bubble sweep-down is the URANIA.

3.1 Computational domain and panel grids used for steady potential flow calculations

The computational domain for the free surface is defined within 1 hull length upstream, 3 lengths downstream and 1.5 lengths aside. One panel grid triplet is used, as summarized in Tab. 1.

Table 1: Panel grids used for the simulations.

Grid ID	Hull Grid	Domain dimension (5.0x1.5)			Total
		Upstream	Hull side	Downstream	
G1	150x50	30x44	30x44	90x44	14k
G2	106x35	21x31	21x31	64x31	7k
G3	75x25	15x22	15x22	45x22	3.5k

Figures 1 and 2 show the body grids (G1, G2 and G3) and the free-surface grids, respectively.

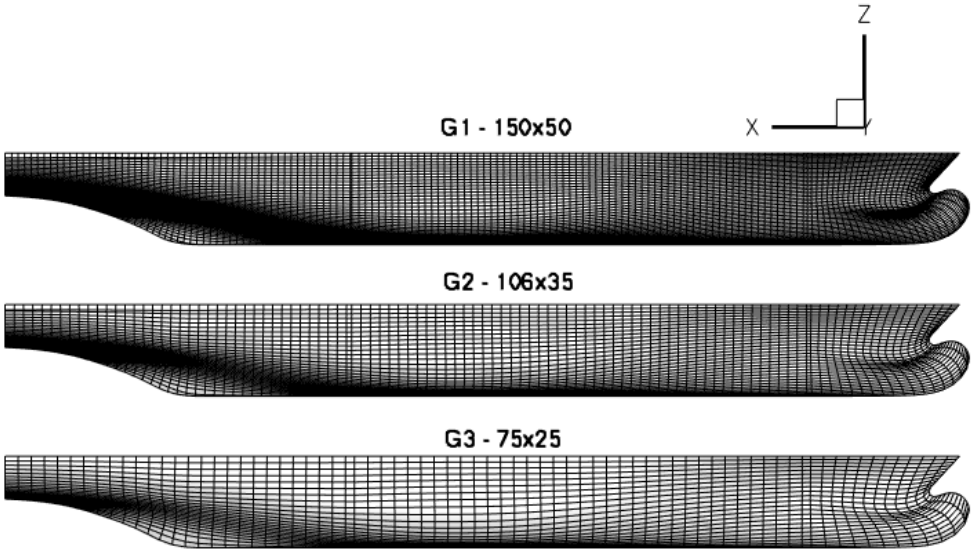

Fig. 1: Body panel grids (G1,G2 and G3)

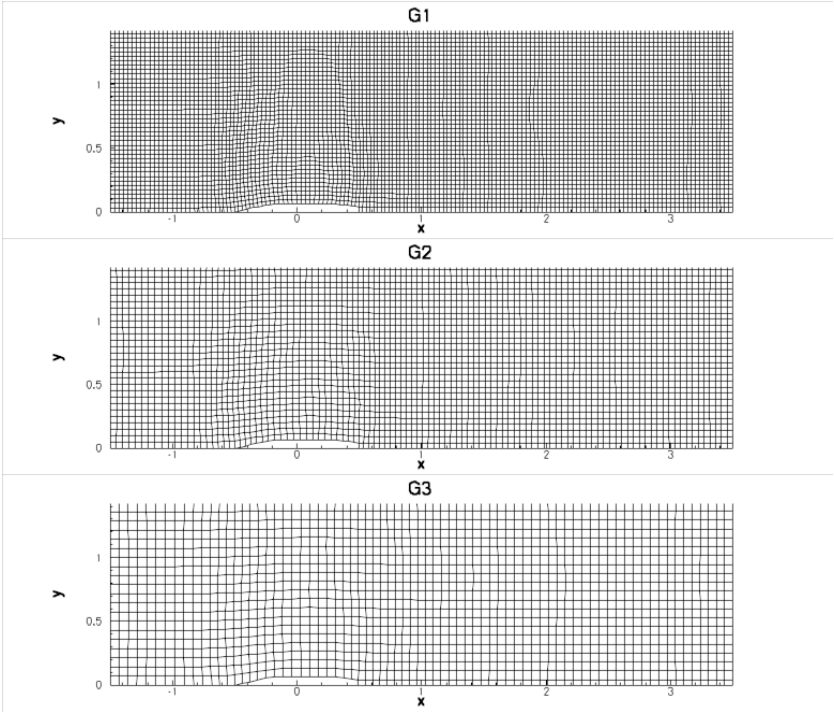

Fig. 2: Free-surface grids (G1,G2 and G3)

Grid convergence and computational domain analyses have been conducted considering the numerical model advancing in calm water, free to sink and trim (2DOFs problem). The fluid conditions are: ρ = 1025 kg/m^3, v = 1.2E-06 m^2/s and g = 9.81 m/s^2.

The main geometrical and operative particulars of the full-scale model, represented in Fig. 3, are summarized in Tab. 2.

Table 2: Model main particulars (full scale).

Description	**Symbol**	**Value**	**Unit**
Displacement	Δ	1200	Tons
Length overall	L_{OA}	61.50	m
Beam overall	B_{OA}	11.10	m
Length between perpendiculars	L_{PP}	52.50	m
Medium draft	T	3.30	m

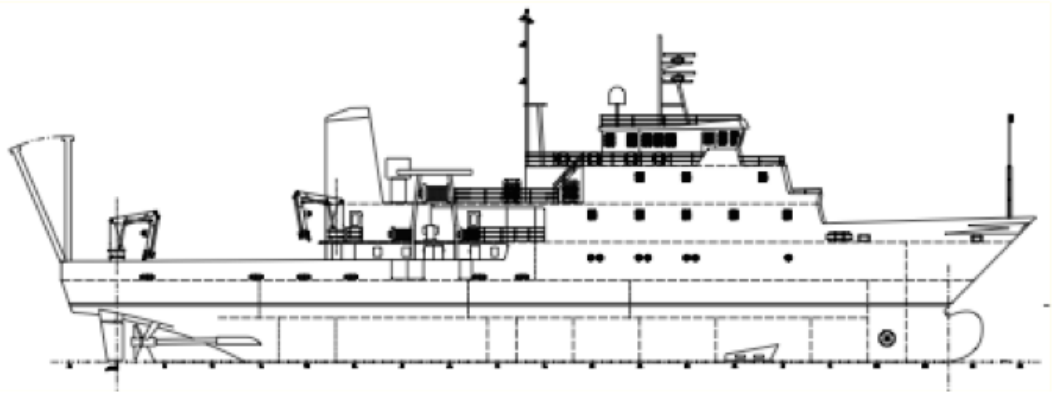

Fig. 3: Longitudinal view of the hull with bulb used as reference (URANIA)

3.2 Steady potential flow results

Potential flow results for the three panel grids are presented in terms of resistance coefficients versus the Froude number (Fr=v/√gLWL) varying from 0.19 to 0.35 (corresponding to 8[kn]≤v≤12[kn]). Figures 4 and 5 depict respectively the wave and the total resistance coefficients evaluated for G1, G2 and G3. Sinkage and trim trends are presented in Figs. 6 and 7. The solution changes are small and the results are grid convergent.

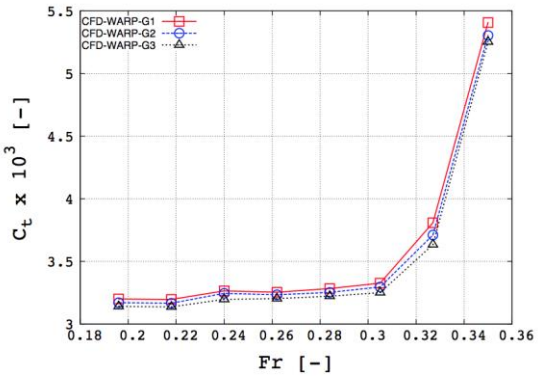

Fig. 4: Wave resistance coefficient

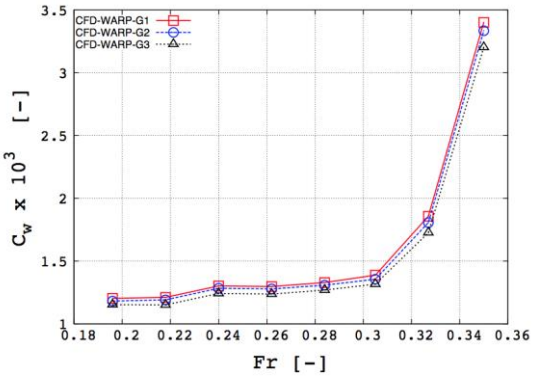

Fig. 5: Friction resistance coefficient

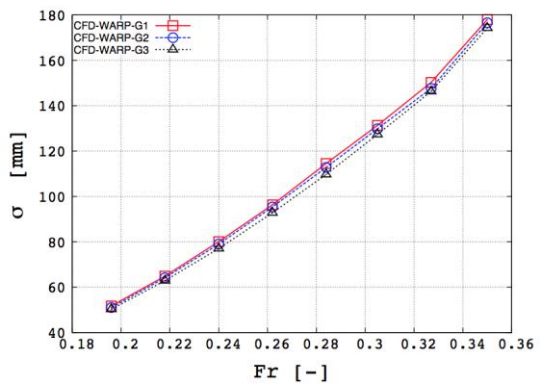

Fig. 6: Sinkage

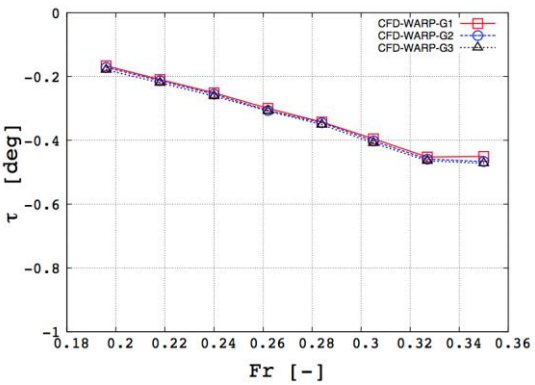

Fig. 7: Trim

The non-dimensional wave elevation is shown, evaluated on the finer grid, for 8[kn]≤v≤12[kn] in Figs. 8-12, respectively.

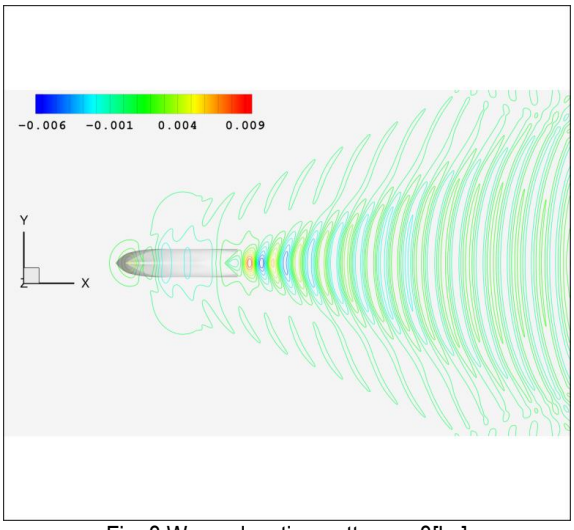

Fig. 8 Wave elevation pattern v=8[kn]

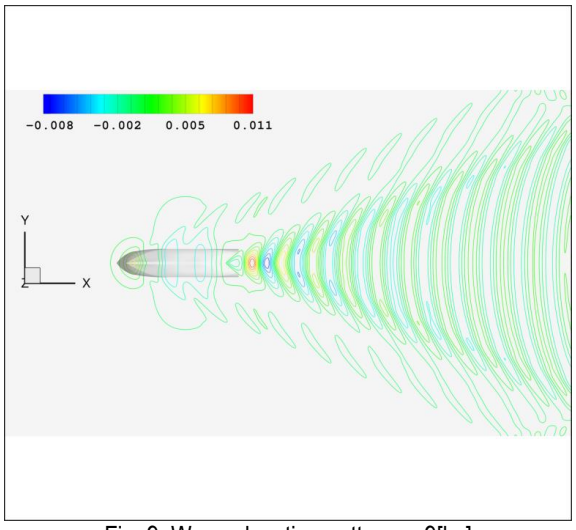

Fig. 9: Wave elevation pattern v=9[kn]

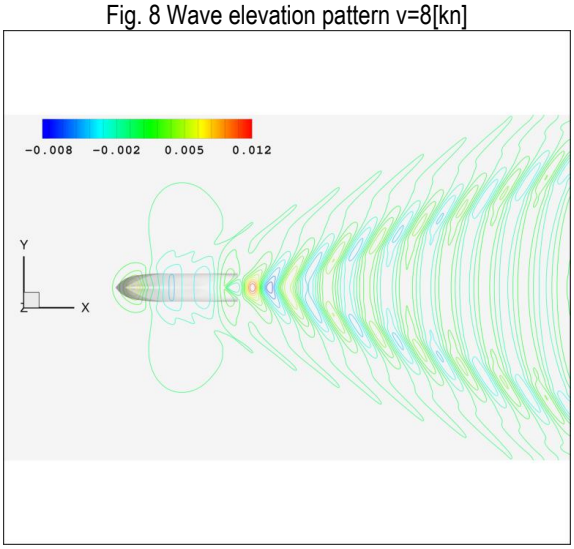

Fig. 10: Wave elevation pattern v=10[kn]

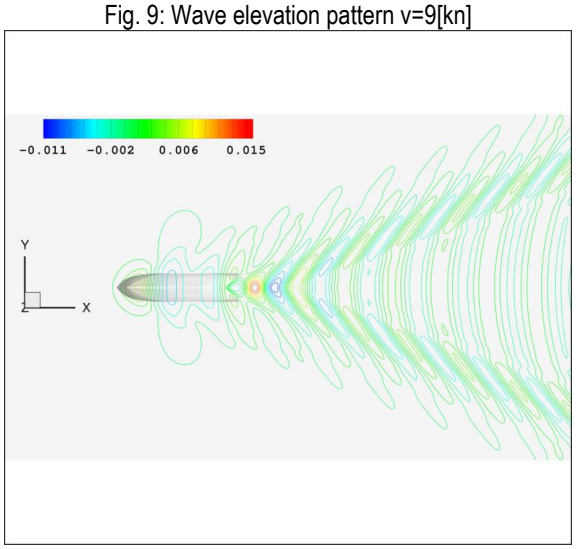

Fig. 11: Wave elevation pattern v=11[kn]

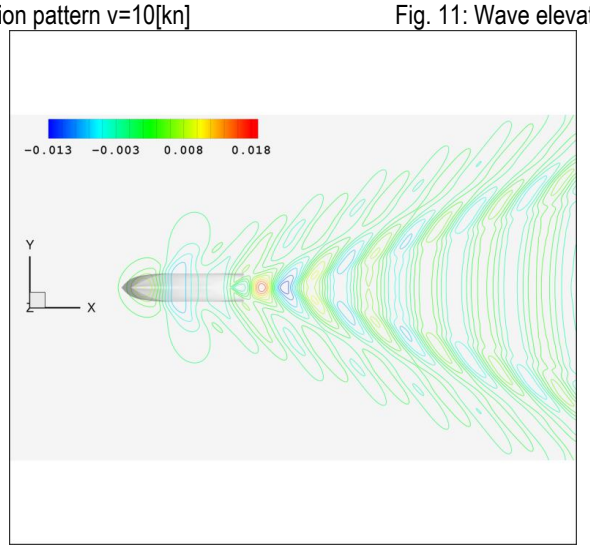

Fig. 12: Wave elevation pattern v=12[kn]

3.3 Seakeeping predictions

The seakeeping performance sensitivity to the grid is shown in this section. Heave and pitch amplitude RAOs, for the three grids, are compared for 8[kn]≤v≤12[kn] and SS6, considering incoming head waves respectively in Figs. 13-17 and Figs. 18-22. The solution changes are small and the results are grid convergent.

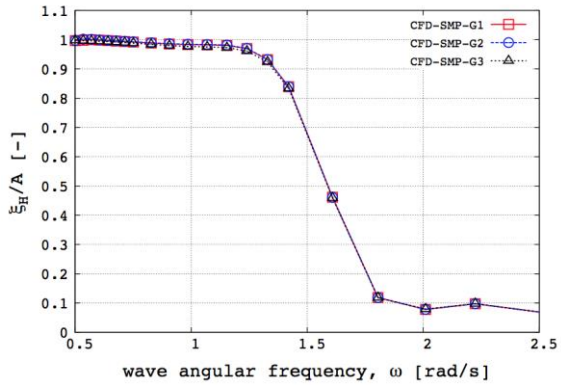

Fig. 13: RAO - heave amplitude v=8[kn]

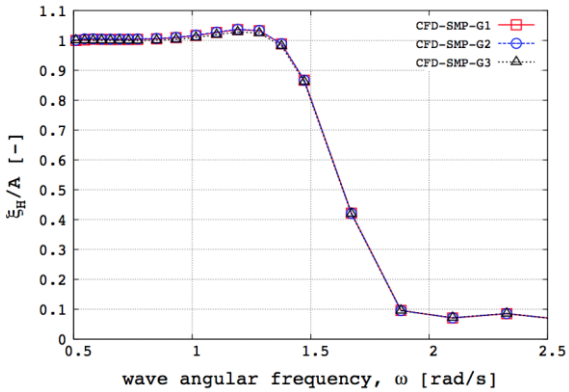

Fig. 14: RAO - heave amplitude v=9[kn]

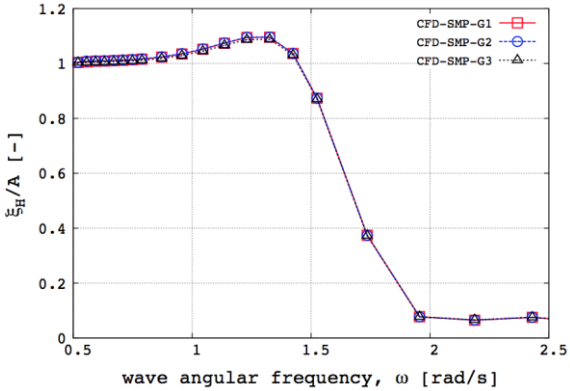

Fig. 15: RAO - heave amplitude v=10[kn]

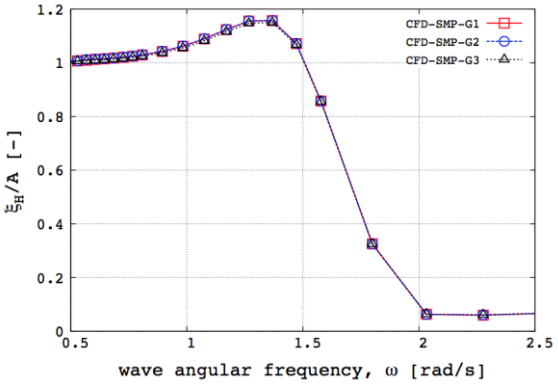

Fig. 16: RAO - heave amplitude v=11[kn]

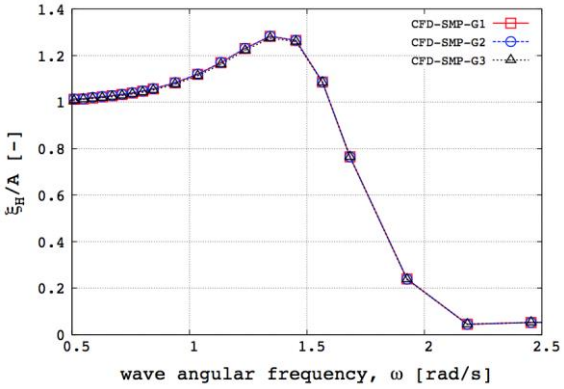

Fig. 17: RAO - heave amplitude v=12[kn]

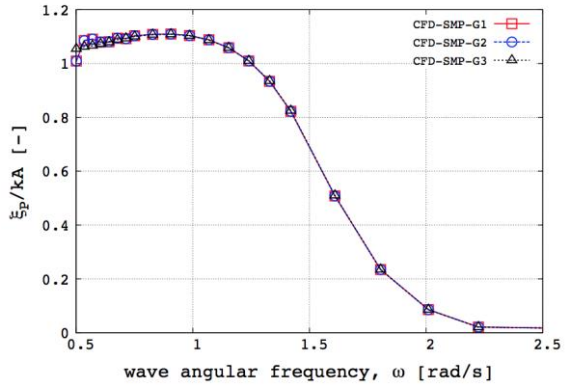

Fig. 18: RAO - pitch amplitude v=8[kn]

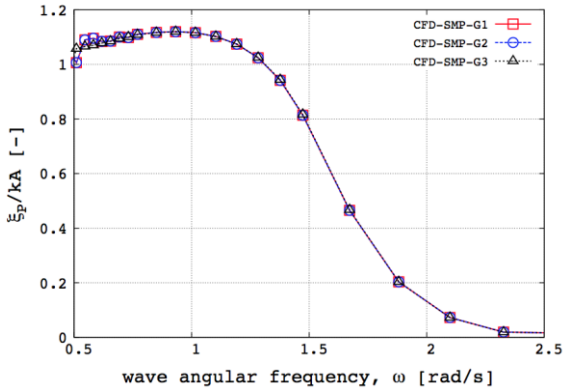

Fig. 19: RAO - pitch amplitude v=9[kn]

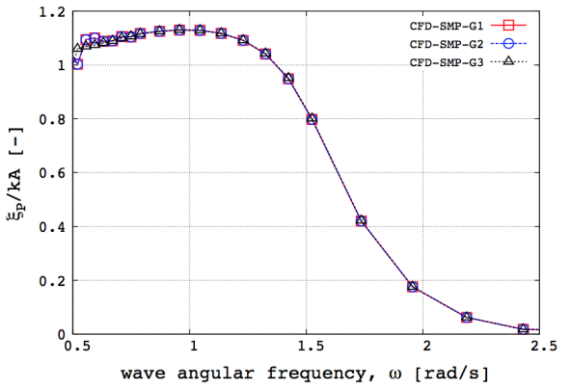

Fig. 20: RAO - pitch amplitude v=10[kn]

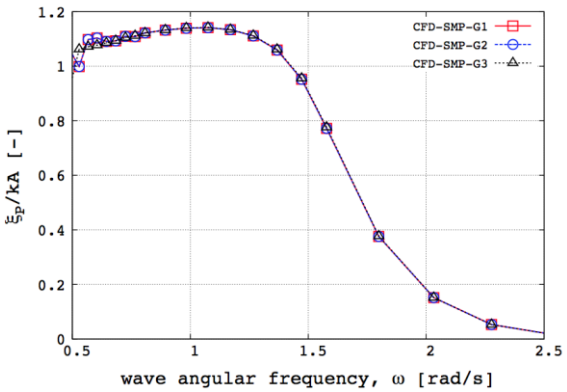

Fig. 21: RAO - pitch amplitude v=11[kn]

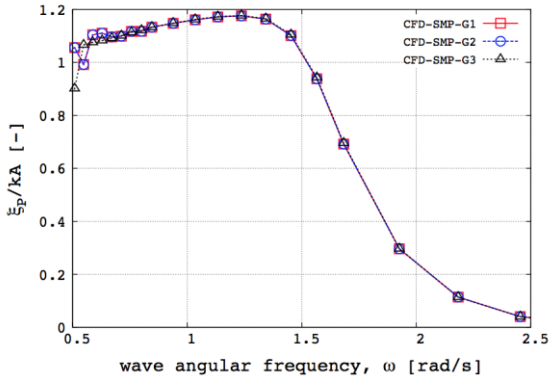

Fig. 22: RAO - pitch amplitude v=12[kn]

3.4 Definition of geometry modifications and design variables

Four orthogonal basis functions and associated design variables are used to modify the hull shape, whereas two functions/variables are used for the bulb, as summarized in Tab. 5 (see for reference Eqs. (1) and (2)).

The design space is investigated using:

1. two patches (see Tab. 5, j=1;3), which are characterized by a first order function over the entire hull. The shape modification consists in moving volume back/front (Fig. 23(a)) and down/up (Fig. 23(c));
2. two additional patches (see Tab. 5, j=2;4), which introduce a higher-order representation of the hull modifications. Volume is moved back/front (Fig. 23(b)) and down/up (Fig. 23(d));
3. two patches controlling the design of the bulb (see Tab. 5, j=5;6), reducing/increasing its width (Fig. 23(e)) and moving it up/down (Fig. 23(f)).

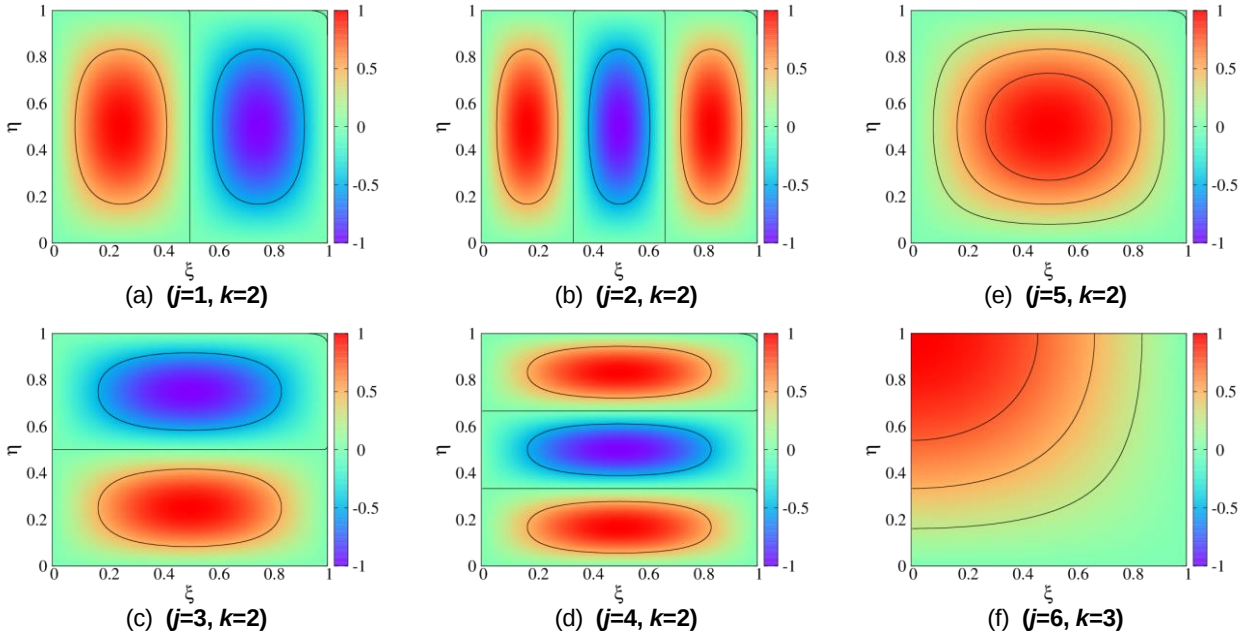

Figure 23: Orthogonal basis function $\psi_j(\xi,\eta)$ for the 6 design variables.

Table 5: Summary of the patches parameters

							Domain	
Description	j	p_j	ϕ_j	q_j	χ_j	k(j)	$\alpha_{j,\min};\alpha_{j,\max}$	$x_{j,\min};x_{j,\max}$
Hull modification	1	2.0	0	1.0	0	2	-1.0; 1.0	-0.5; 0.5
	2	3.0	0	1.0	0	2	-1.0: 1.0	-0.5; 0.5
	3	1.0	0	2.0	0	2	-0.5; 0.5	-0.5; 0.5
	4	1.0	0	3.0	0	2	-0.5: 0.5	-0.5; 0.5
Bulb modification	5	1.0	0	1.0	0	2	-0.25: 0.25	-0.5; 0.5
	6	0.5	$\pi/2$	0.5	0	3	-0.5: 0.5	-0.5; 0.5

Figures 24-35 show the original hull compared with the modified ones. Maximum and minimum variations for each patch (design variable) are shown.

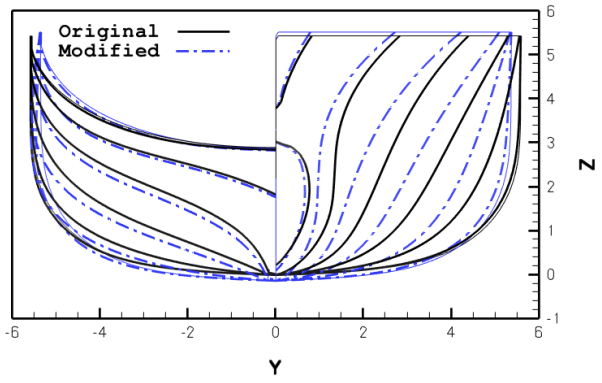

Figure 24: Hull modification with patch 1 - x_{MIN}=-0.5

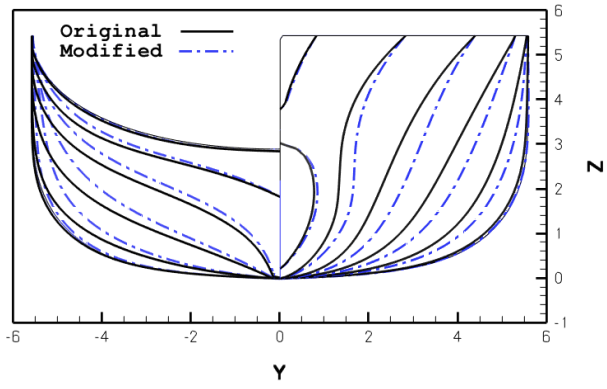

Figure 25: Hull modification with patch 1 – x_{MAX}=0.5

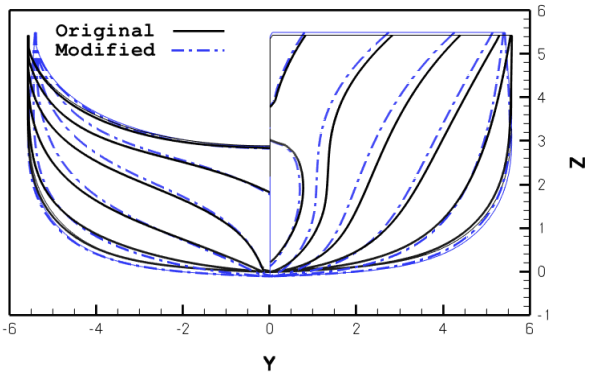

Figure 26: Hull modification with patch 2 - x_{MIN}=-0.5

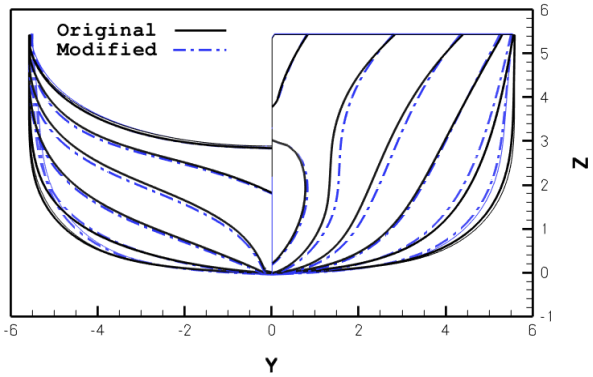

Figure 27: Hull modification with patch 2– x_{MAX}=0.5

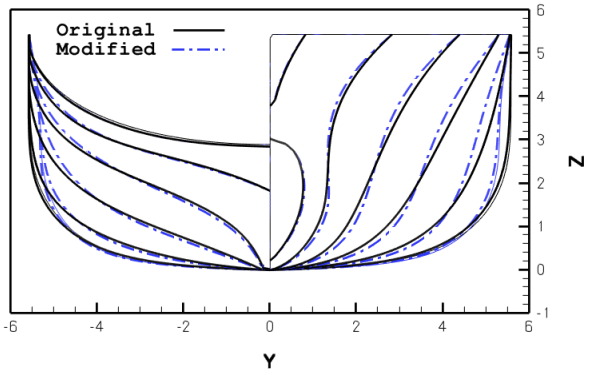

Figure 28: Hull modification with patch 3 - x_{MIN}=-0.5

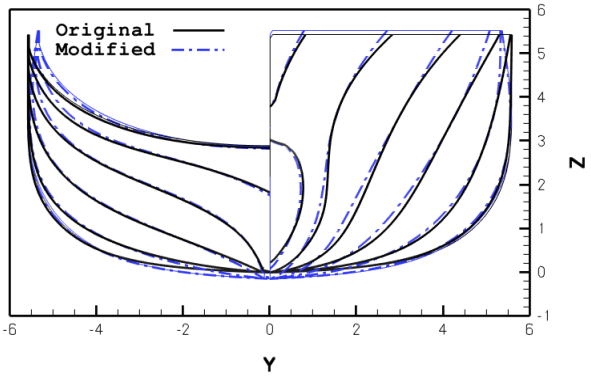

Figure 29: Hull modification with patch 3 – x_{MAX}=0.5

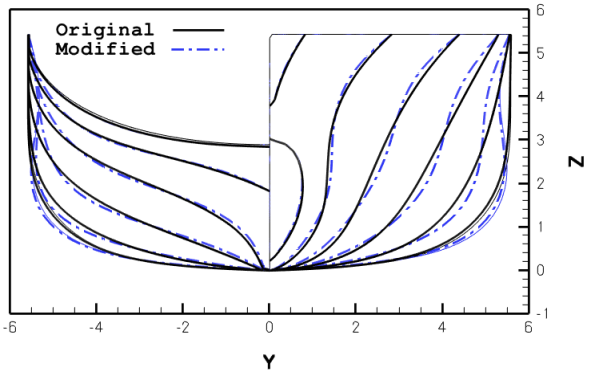

Figure 30: Hull modification with patch 4 - x_{MIN}=-0.5

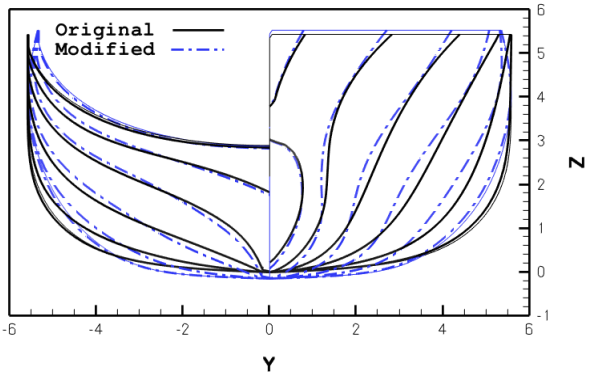

Figure 31: Hull modification with patch 4 – x_{MAX}=0.5

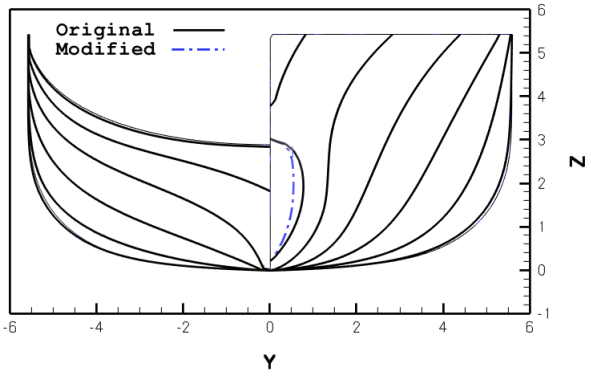

Figure 32: Hull modification with patch 5 - x_{MIN}=-0.5

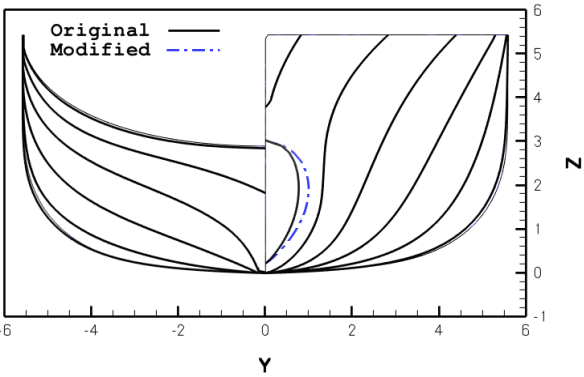

Figure 33: Hull modification with patch 5 – x_{MAX}=0.5

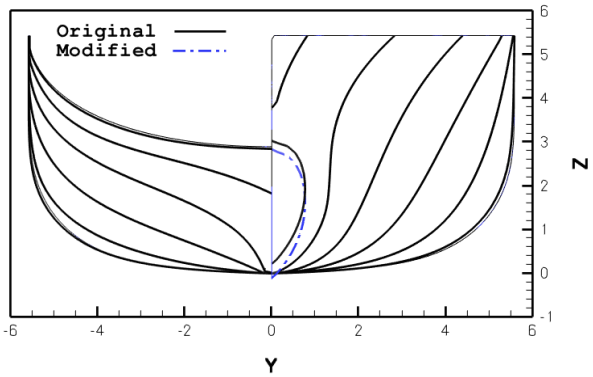

Figure 34: Hull modification with patch 6 - x_{MIN}=-0.5

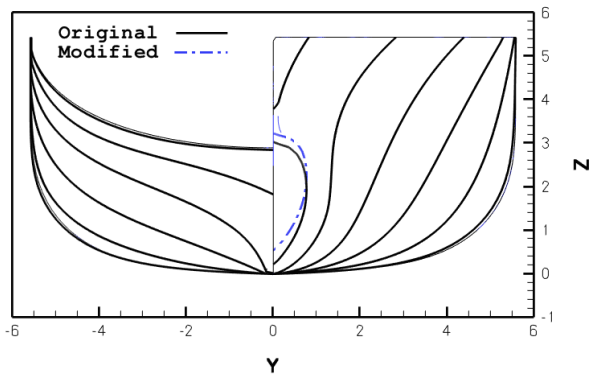

Figure 35: Hull modification with patch 6– x_{MAX}=0.5

Summarizing, patches 1 and 2 modify the shape allowing for volume movement from back to front of the hull, patches 3 and 4 control volume modification from up to down, patch 5 controls the increase/decrease of the bulb whereas patch 6 moves the bulb up and down.

3.5 Sensitivity analysis to F1

The sensitivity analysis of F1 to the shape modifications is performed in calm water at Fr=0.218 (10 [kn]). The overall objective function F1, representing the mean downwards vertical speed component at the bow, evaluated in calm water at 10[kn], is studied (see Fig. 36).

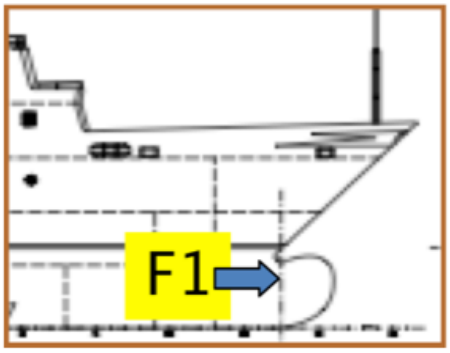

Figure 36: Location of F1 evaluation

Figure 37 shows the independent effects of the hull and bulb shapes modifications - defined in order to move volumes aft/forward (x_1,x_2), down/up (x_3,x_4), decrease/increase of bulb width (x_5) and move bulb down/up (x_6) - on the objective F1. Negative values of ΔF allow for improvements and unfeasible designs are not reported. Specifically, positive values of design variables 1 and 3, which means moving volume back to front and up to down (using a p=2 order) always result in an increase of performances, whereas positive values of variables 2,4, 5 and 6, which mean moving volume back to front and up to down (using a p=3 order), increasing bulb width, and raising it up lead to a performance decrease.

The sensitivity analysis for the F1 shows a possible reduction of the objective function close to 5%.

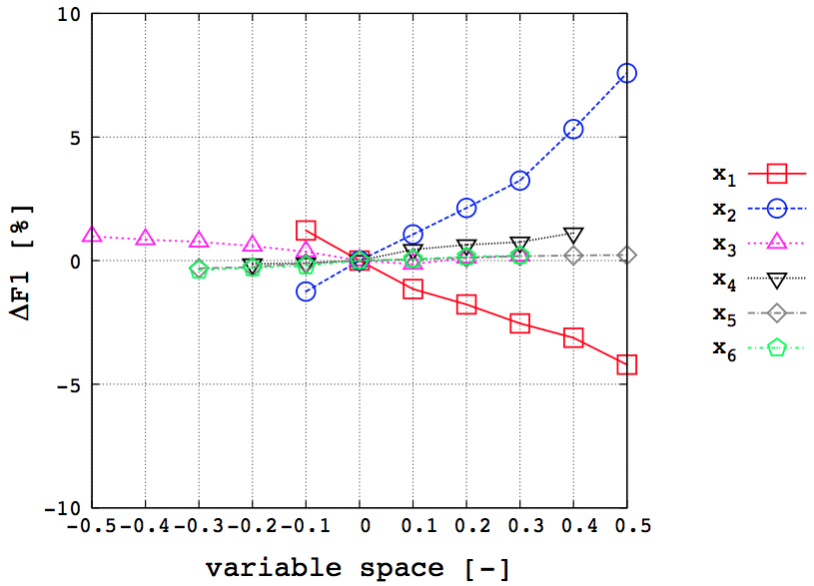

Figure 37: Sensitivity analysis to F1

3.6 Design optimization for F1

Design optimization is performed with

- box constraints defined by $-0.5 \leq x_i \leq 0.5$,
- fixed length between perpendiculars and fixed displacement,
- limited variations on beam and draught (+/- 5%),
- reserved volume for the bulb.

The optimization reaches a reduction of the 5.6% of the objective function F1 as in Fig. 38(a). Figure 38(b) presents the values of the corresponding optimal design variables.

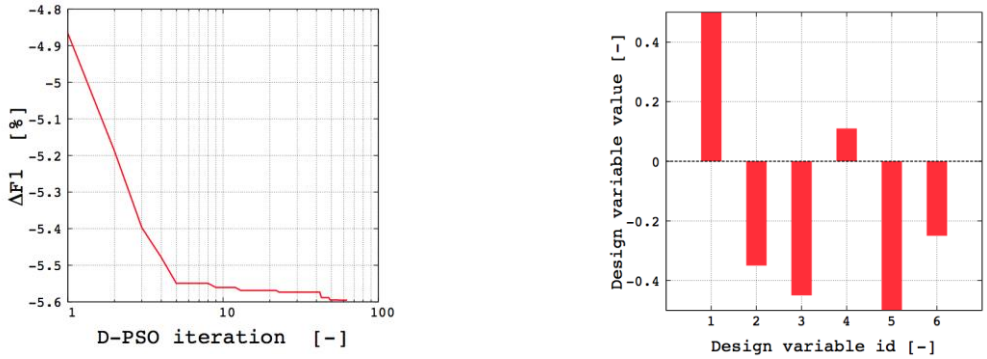

Figure 38: Objective function convergence trend (a) and optimum design variable values (b).

Figure 39 shows the optimized hull shape compared to the original. The reduction of the objective function is consistent with the reduction shown again in Fig. 39, where the mean downward vertical component of the speed is presented along with the streamlines on the optimized hull compared to the original.

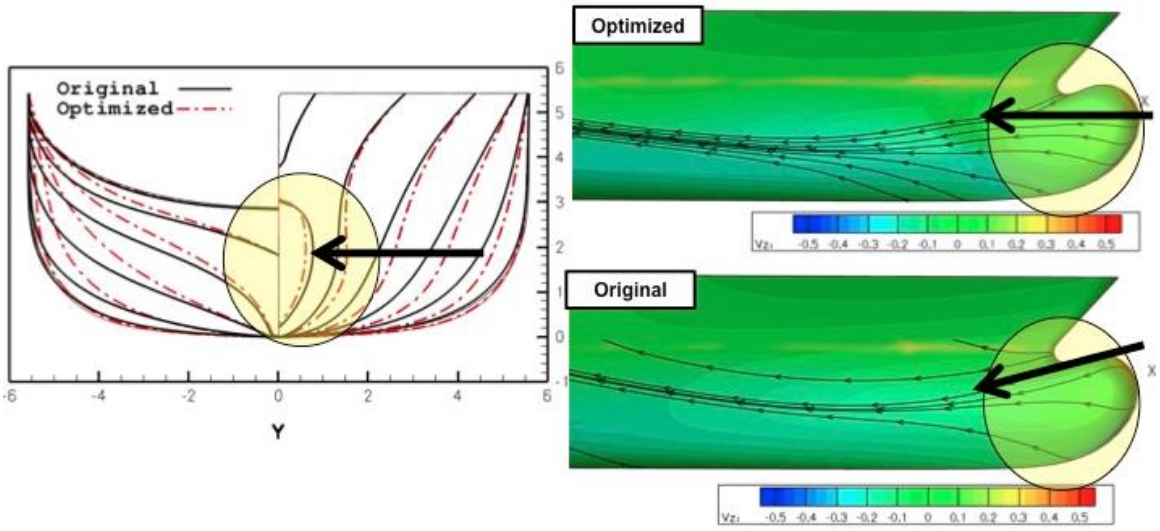

Figure 39: Optimal (red) shape compared to the original (black) and streamlines trend for optimal and original configurations

The result of the optimization shows that a narrow bulb allows for decreasing the local mean downward speed component.

3.7 Sensitivity analysis to F2

Seakeeping sensitivity analysis of F2 to shape modifications is performed with SMP. The overall objective function F2, that represents the RMS of the vertical acceleration at the bow evaluated at sea state 2 and 6 and for v=10[kn], is studied (see Fig. 40).

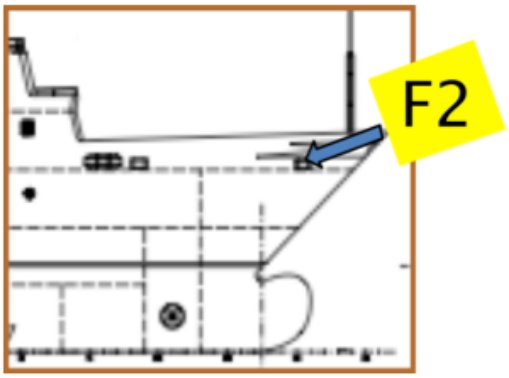

Figure 40: Location of F2 evaluation

Figure 41 shows the sensitivity analysis for the normalized RMS of vertical acceleration of the bow (using a Bretschneider spectrum with a significant wave height equal to 0.3[m] and 5.0[m] and a modal period equal to 3.8[s] and 9.8[s], respectively for sea-state 2 and 6), unfeasible designs are not reported. Specifically, positive values of design variables, which means moving volume back to front and up to down, always result in seakeeping performance improvements.

The results show a possible reduction of the objective function close to 10%.

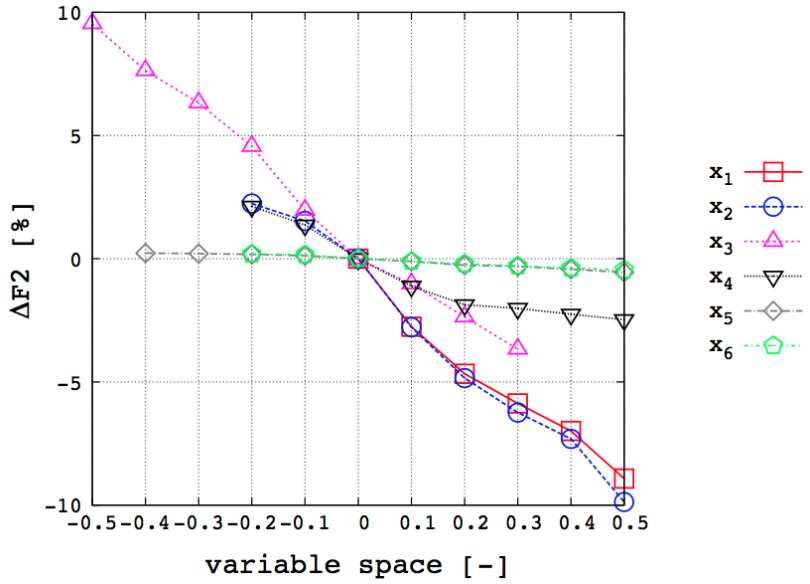

Figure 41: Sensitivity analysis to F2

3.8 Design optimization for F2

Design optimization is performed with

- box constraints defined by $-0.5 \leq x_i \leq 0.5$,
- fixed length between perpendiculars and fixed displacement,
- limited variations on beam and draught (+/- 5%),
- reserved volume for the bulb.

The optimization reaches a reduction of the 9.3% of the objective function F2 as in Fig. 42(a). Figure 42(b) presents the values of the corresponding optimal design variables.

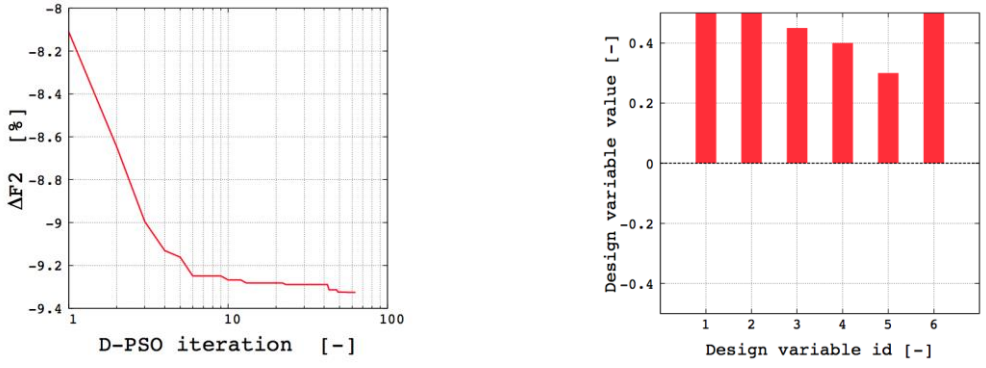

(a) (b)

Figure 42: Objective function convergence trend (a) and optimum design variable (b).

Figure 43 shows the optimized hull shape compared to the original. The reduction of the objective function is consistent with the reduction shown in Fig. 43, where the RAOs of heave and pitch for the optimized configuration are also compared to the original ones.

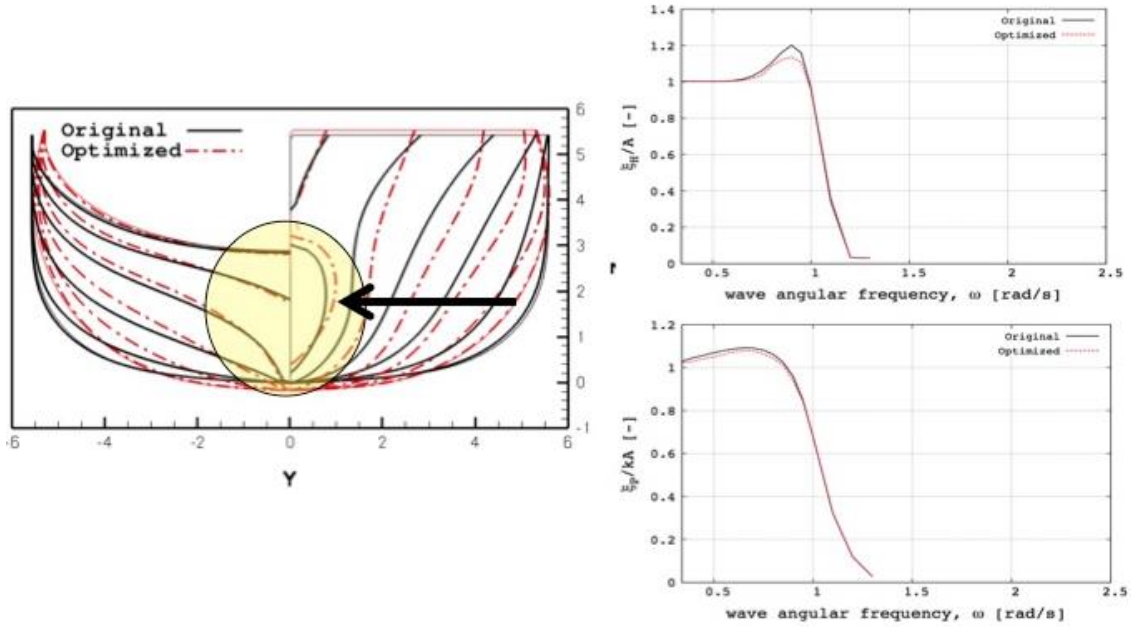

Figure 43: Optimal (red) shape compared to the original (black) and Optimal shape *vs* original heave and pitch RAOs

3.9 Multi-objective design optimization

The selection of the optimal hull on the Pareto front (blue point) comes from the best compromise between the two objective functions. Considering the Pareto front achieved, a possible reduction of F1 in between 2.5 and 6% associated with 3 to 10.5% of reduction of F2 considering box constraints defined by $-0.5 \leq x_j \leq 0.5$.

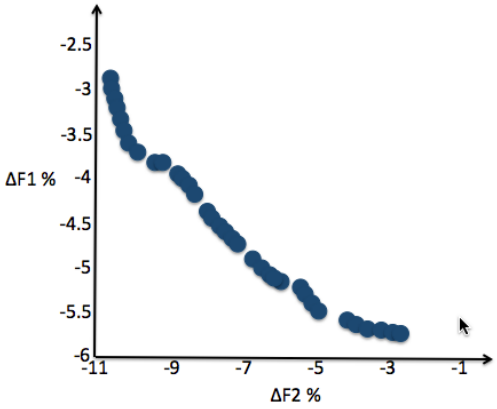

Figure 44: Multi-objective optimization result

4. Hull without bulb

The original hull without bulb selected to derive indications on the proper design to mitigate bubble sweep-down is the RRV50, whose design has been developed during the current project (see D11.4 and D11.5).

4.1 Computational domain and panel grids used for steady potential flow calculations

The computational domain for the free surface is defined within 1 hull length upstream, 3 lengths downstream and 1.5 lengths for the side. One panel grid triplet is used, as summarized in Tab. 6.

Table 6: Panel grids used for the simulations.

Grid ID	Hull Grid	Domain dimension (5.0x1.5)			Total
		Upstream	Hull side	Downstream	
G1	100x50	30x44	30x44	90x44	11.6k
G2	71x35	21x31	21x31	64x31	5.8k
G3	50x25	15x22	15x22	45x22	2.9k

Figures 45,47 and 49 show the body grids (G1, G2 and G3), whereas Figs. 46,48 and 50 are the corresponding free-surface grids.

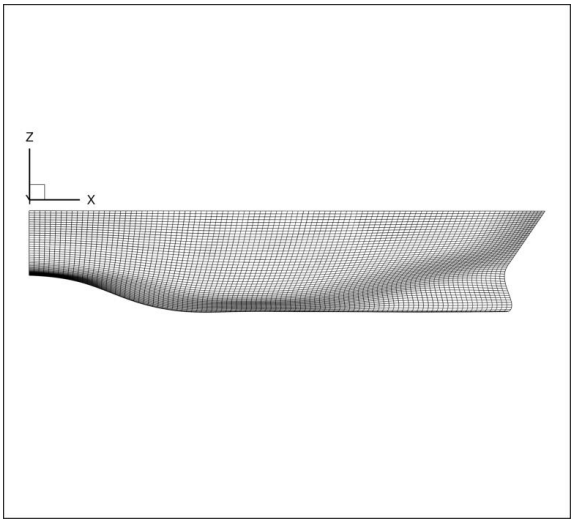

Figure 45: Body panel grid (G1)

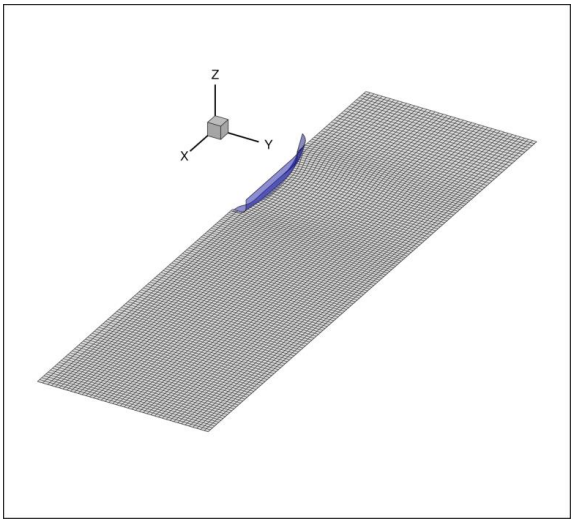

Figure 46: Free-surface panel grid (G1)

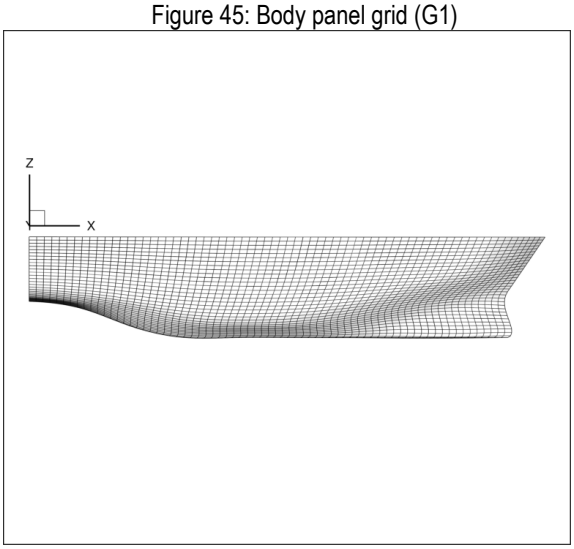

Figure 47: Body panel grid (G2)

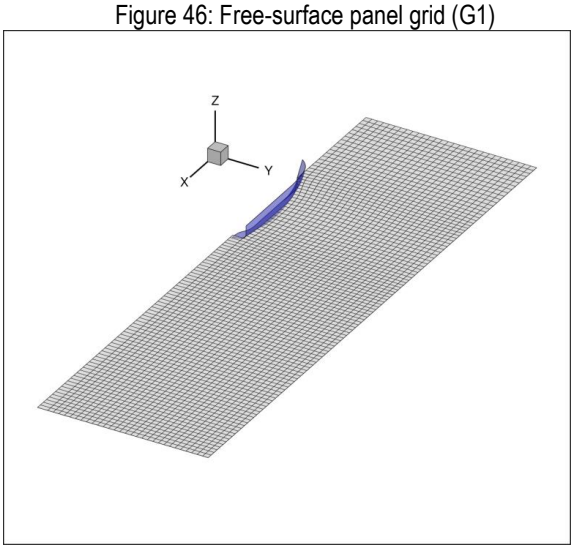

Figure 48: Free-surface panel grid (G2)

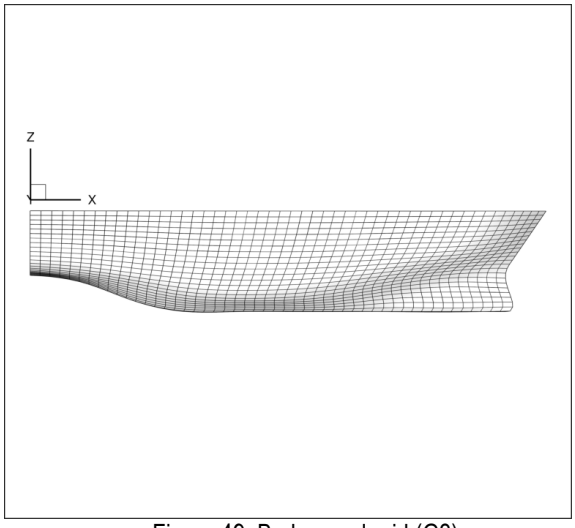

Figure 49: Body panel grid (G3)

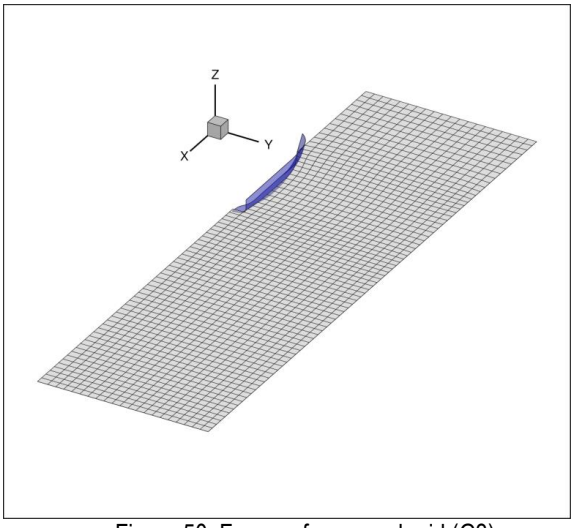

Figure 50: Free-surface panel grid (G3)

Grid convergence and computational domain analyses have been conducted considering the numerical model advancing in calm water, free to sink and trim (2DOFs problem). The fluid conditions are: ρ = 1025 kg/m^3, v = 1.2E-06 m^2/s and g = 9.81 m/s^2.

The main geometrical and operative particulars of the full-scale model, represented in Fig. 51, are summarized in Tab. 7.

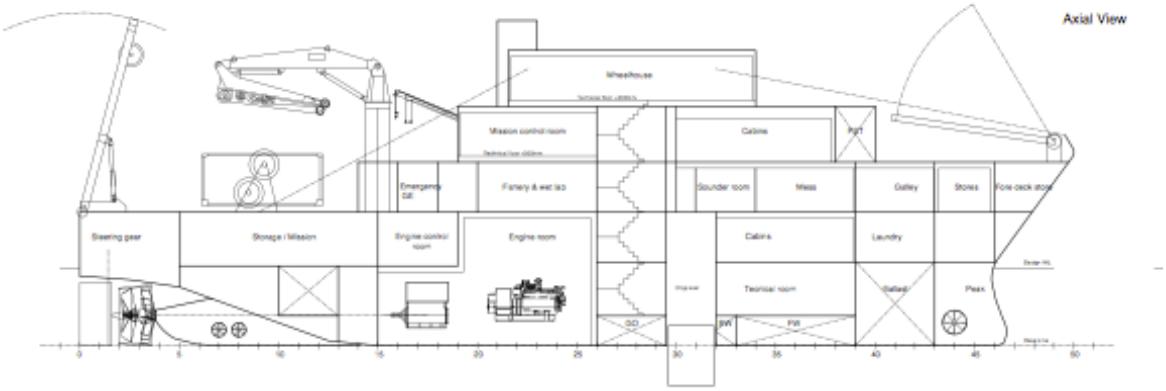

Fig. 51: RRV50 longitudinal view

Table 7: Model main particulars (full scale)

Description	Symbol	Value	Unit
Displacement	Δ	1012.83	Tons
Length at the waterline	L_{WL}	46.78	m
Beam at the waterline	B_{WL}	11.17	m
Medium draft	T	4.05	m
Vertical center of gravity	VCG	5.33	m

Potential flow results for the three panel grids are presented in terms of resistance coefficients versus the Froude number ($Fr=v/\sqrt{gL_{WL}}$) varying from 0.188 to 0.376 (corresponding to 8[kn]≤v≤16[kn]). Figures 52, 53 and

54 depict respectively the wave, the friction and the total resistance coefficients evaluated for G1, G2 and G3. The solution changes are small and the results are grid convergent. Sinkage and trim trends are presented in Figs. 55 and 56. Although the trim trend shows an oscillatory convergence, the current grid G1 is deemed adequate to solve the flow. The dimensional total resistance is shown in Fig. 57, for the finer grid G1.

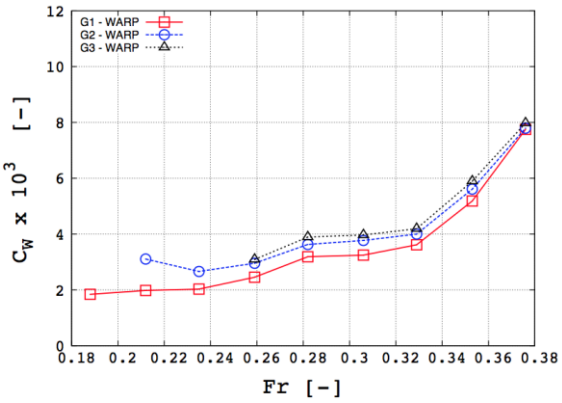

Fig. 52: Wave resistance coefficient

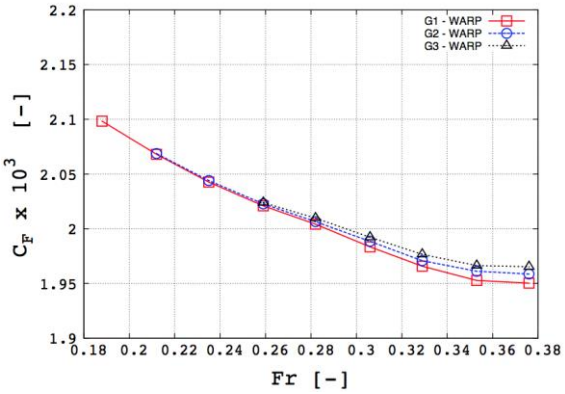

Fig. 53: Friction resistance coefficient

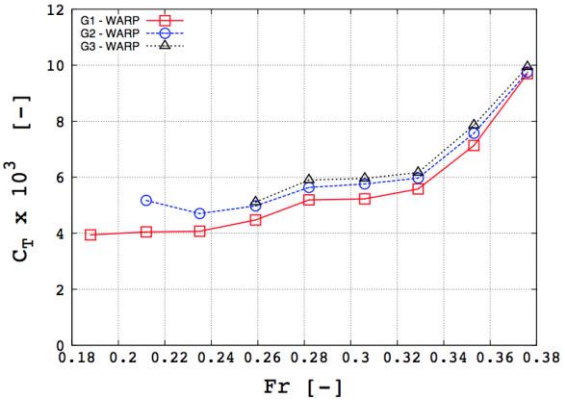

Fig. 54: Total resistance coefficient

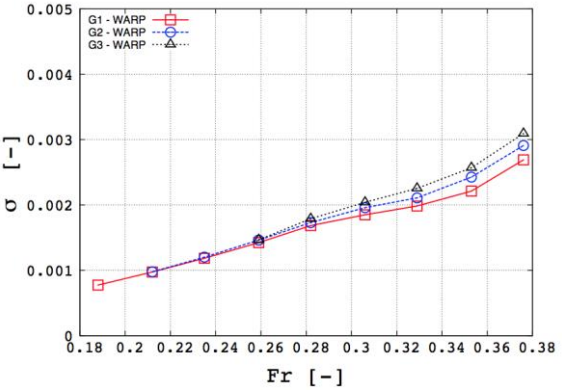

Fig. 55: Sinkage

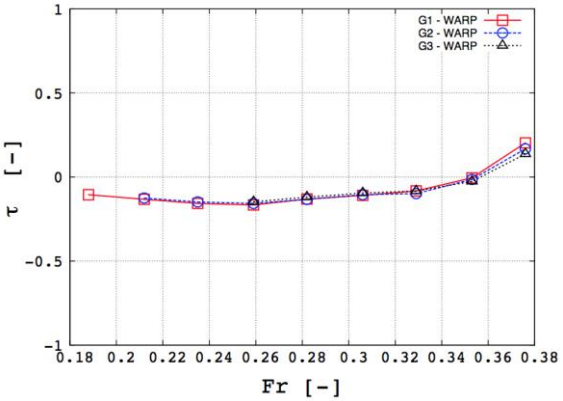

Fig. 56: Trim

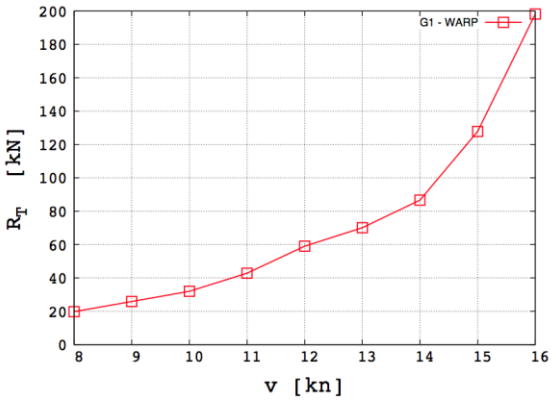

Fig. 57: Total resistance

The non-dimensional wave elevation is shown, evaluated on the finer grid, for 8[kn]≤v≤16[kn] in Figs. 58-66, respectively.

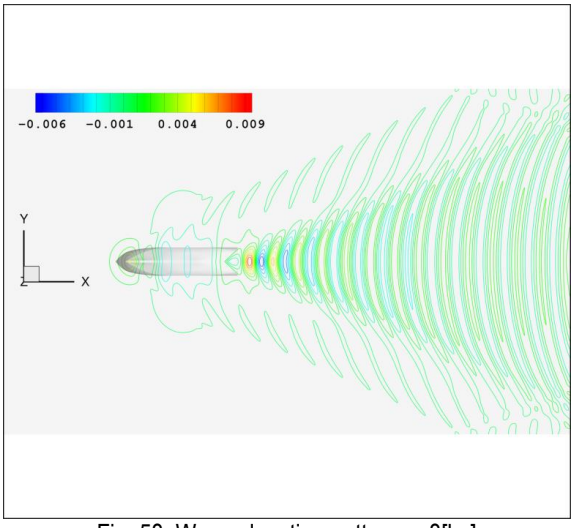

Fig. 58: Wave elevation pattern v=8[kn]

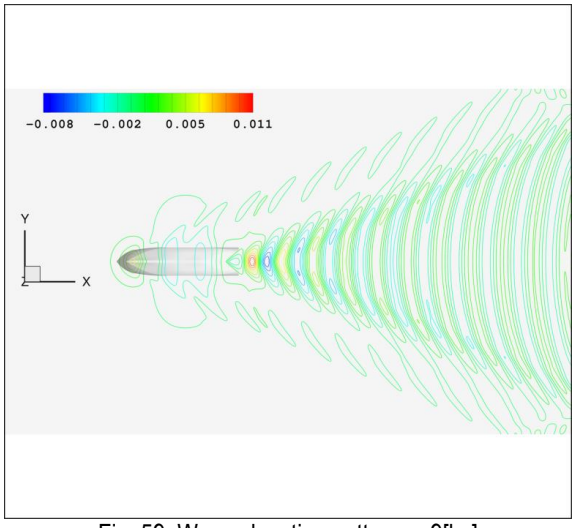

Fig. 59: Wave elevation pattern v=9[kn]

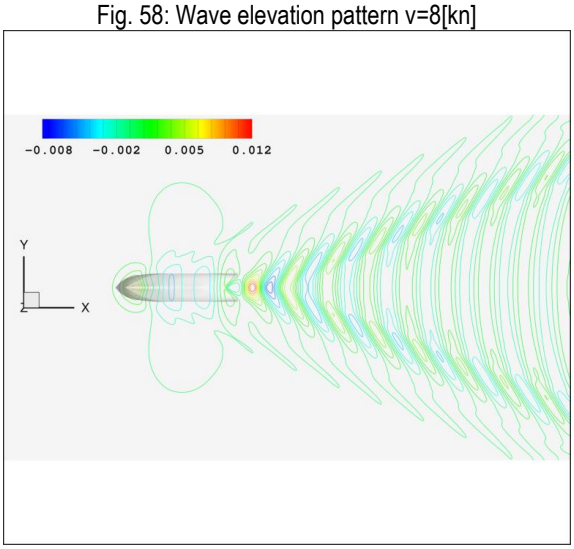

Fig. 60: Wave elevation pattern v=10[kn]

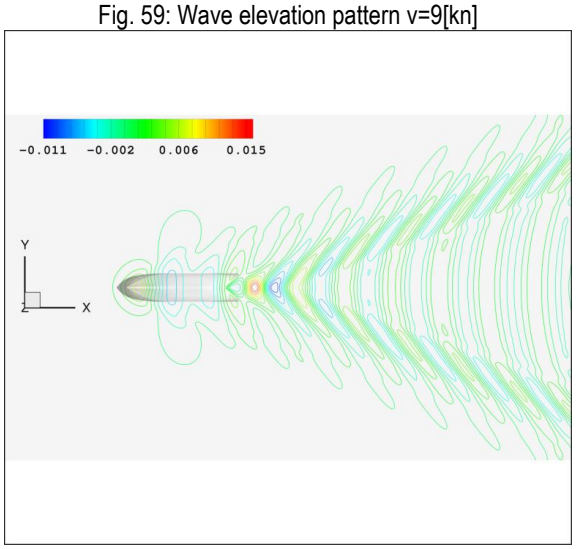

Fig. 61: Wave elevation pattern v=11[kn]

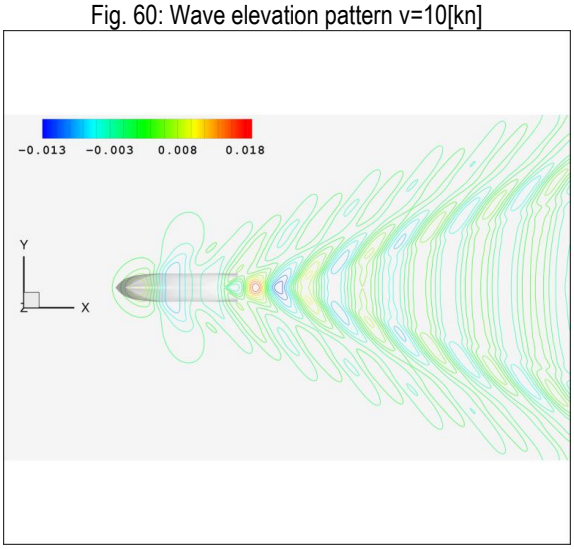

Fig. 62: Wave elevation pattern v=12[kn]

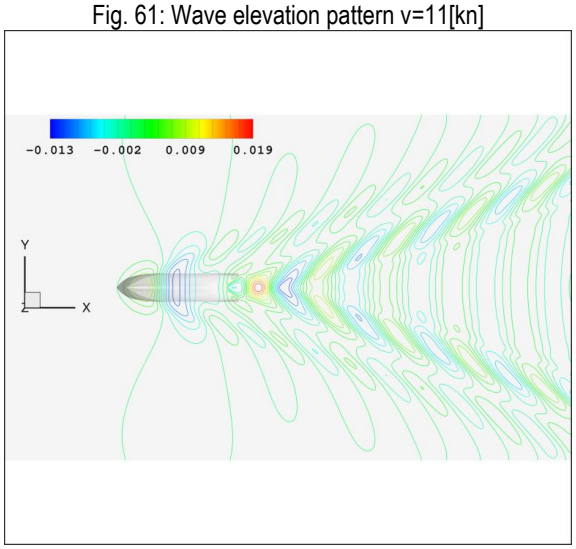

Fig. 63: Wave elevation pattern v=13[kn]

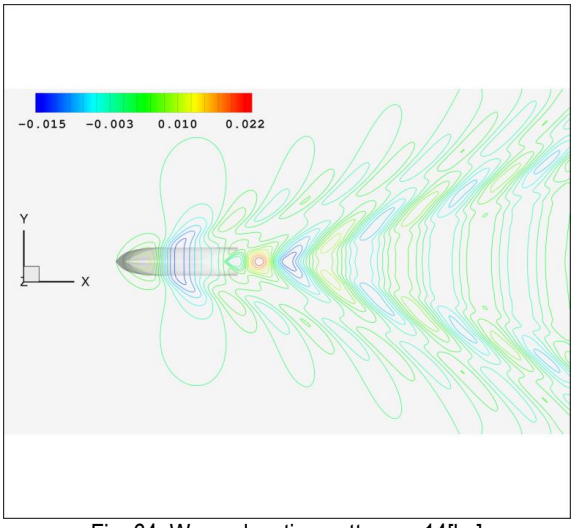

Fig. 64: Wave elevation pattern v=14[kn]

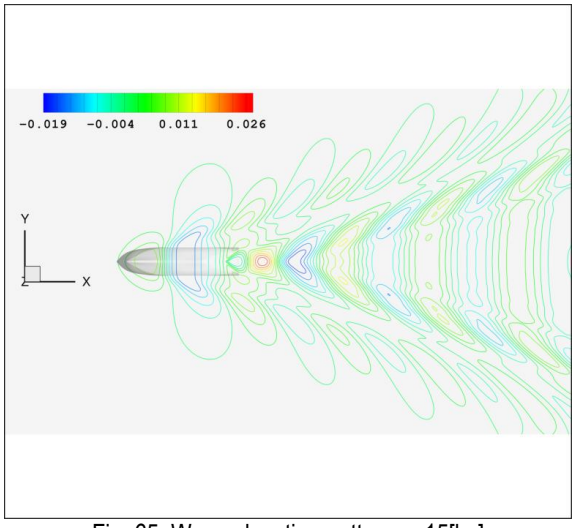

Fig. 65: Wave elevation pattern v=15[kn]

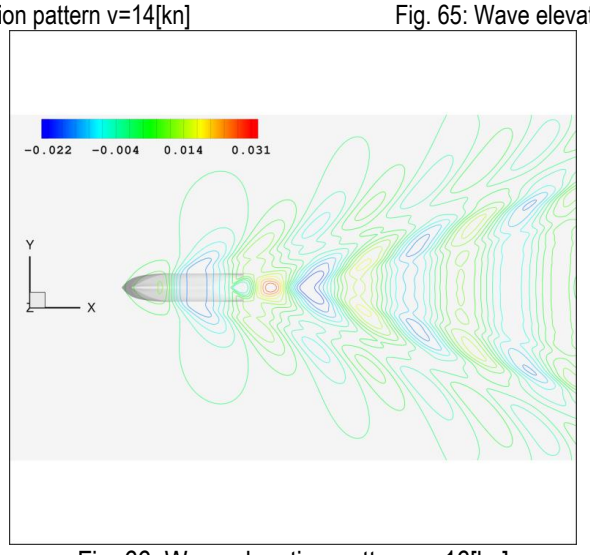

Fig. 66: Wave elevation pattern v=16[kn]

The non-dimensional pressure distributions are presented in Figs. 67-75, for 8[kn]≤v≤16[kn].

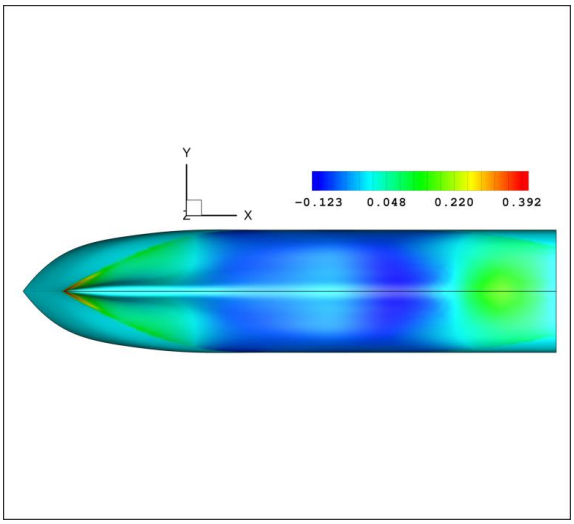

Fig. 67: Non-dimensional pressure distribution v=8[kn]

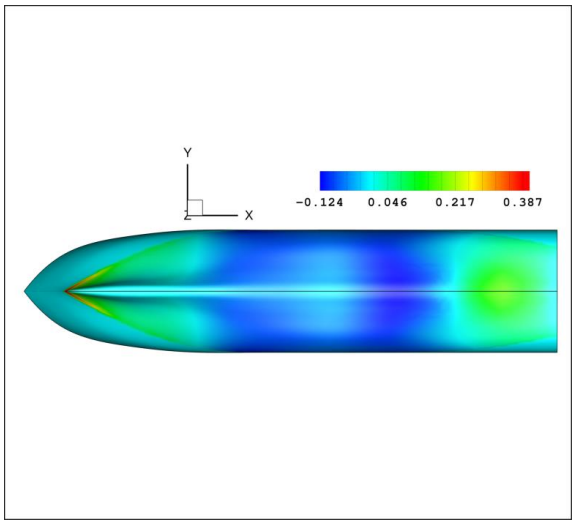

Fig. 68: Non-dimensional pressure distribution v=9[kn]

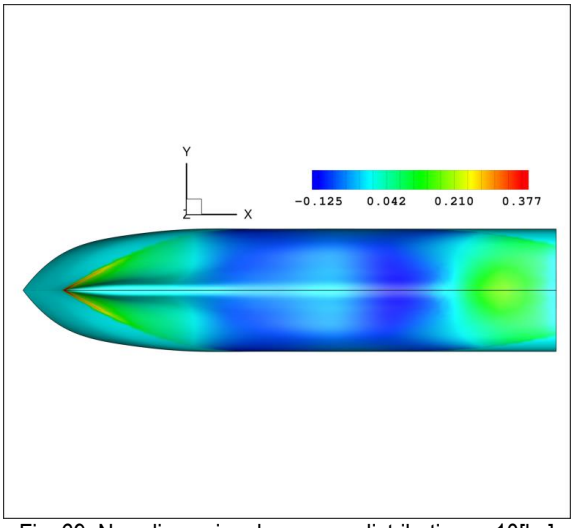

Fig. 69: Non-dimensional pressure distribution v=10[kn]

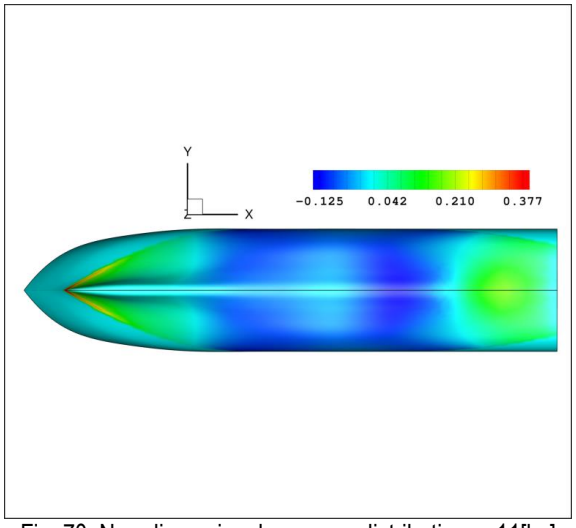

Fig. 70: Non-dimensional pressure distribution v=11[kn]

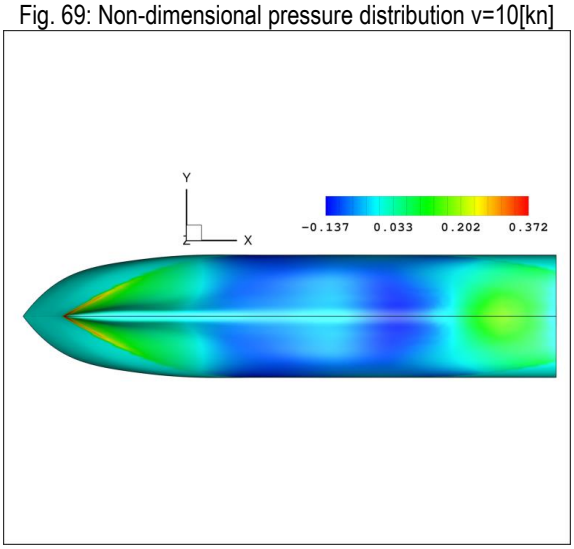

Fig. 71: Non-dimensional pressure distribution v=12[kn]

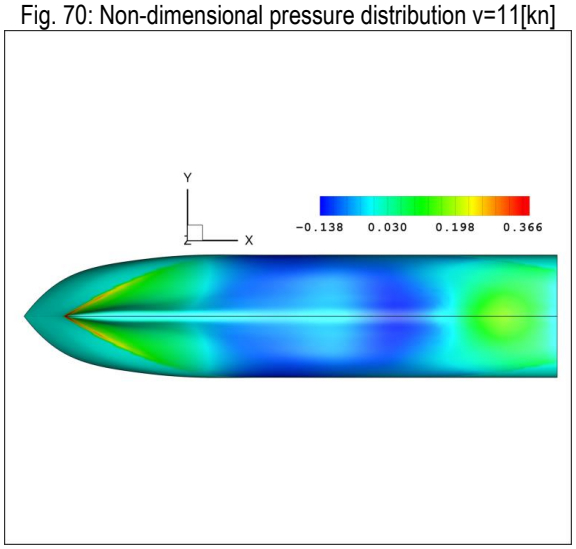

Fig. 72: Non-dimensional pressure distribution v=13[kn]

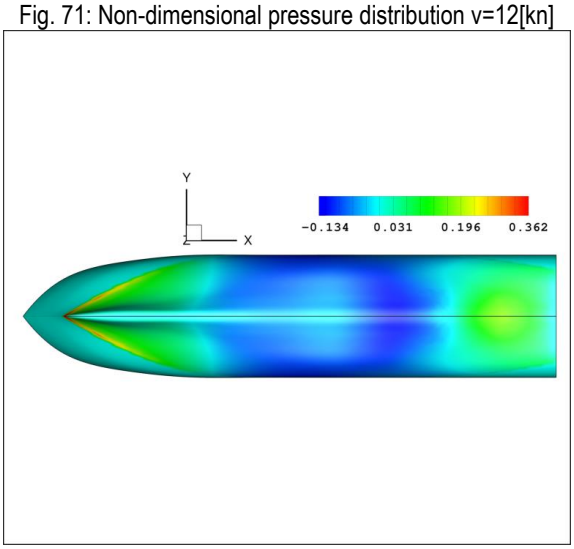

Fig. 73: Non-dimensional pressure distribution v=14[kn]

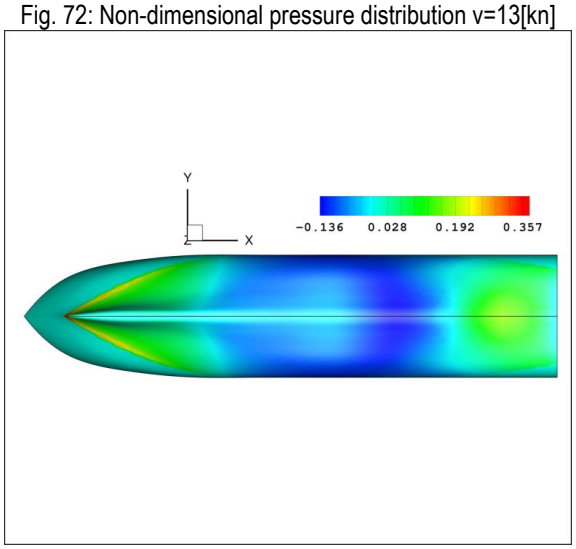

Fig. 74: Non-dimensional pressure distribution v=15[kn]

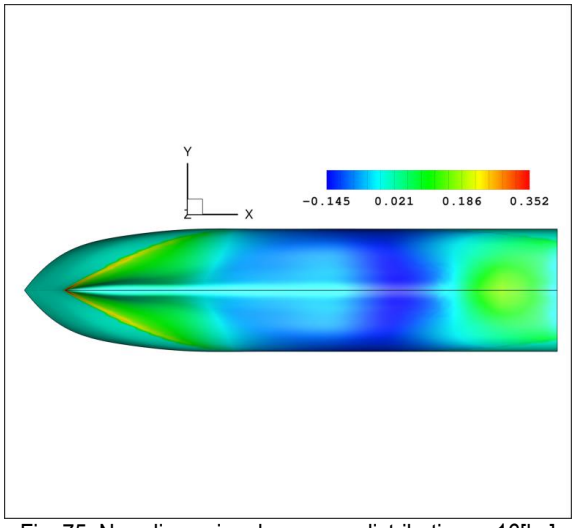

Fig. 75: Non-dimensional pressure distribution v=16[kn]

The vertical component of the speed v_z distributions are presented in Figs. 76-84, for 8[kn]≤v≤16[kn].

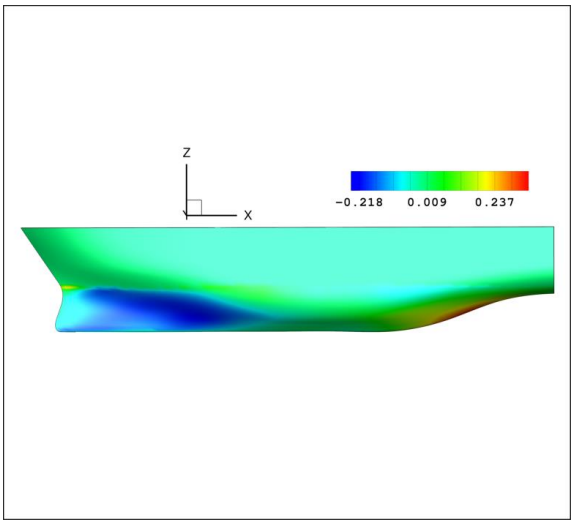

Fig. 76: Vertical speed component v_z v=8[kn]

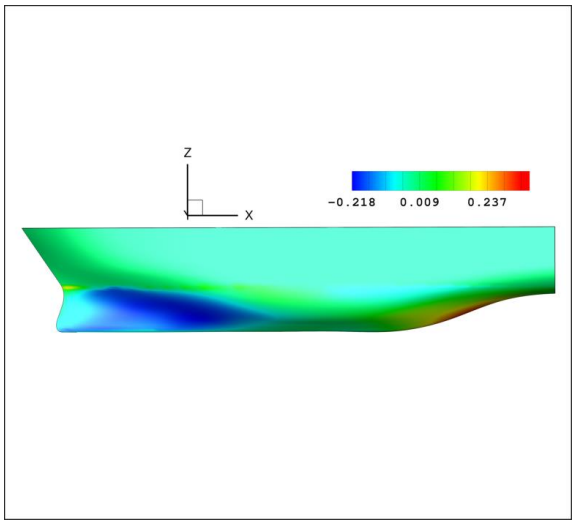

Fig. 77: Vertical speed component v_z v=9[kn]

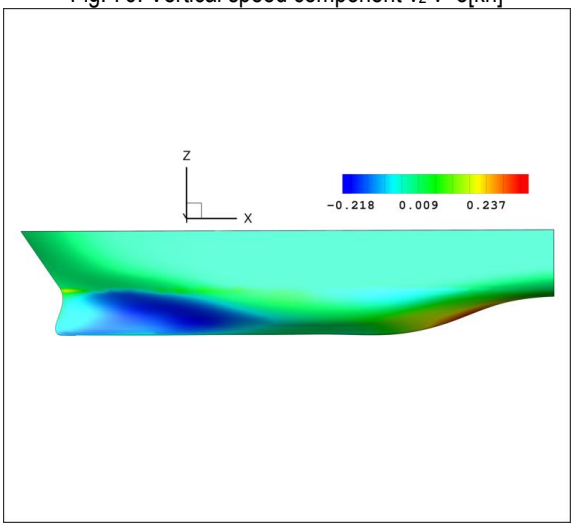

Fig. 78: Vertical speed component v_z v=10[kn]

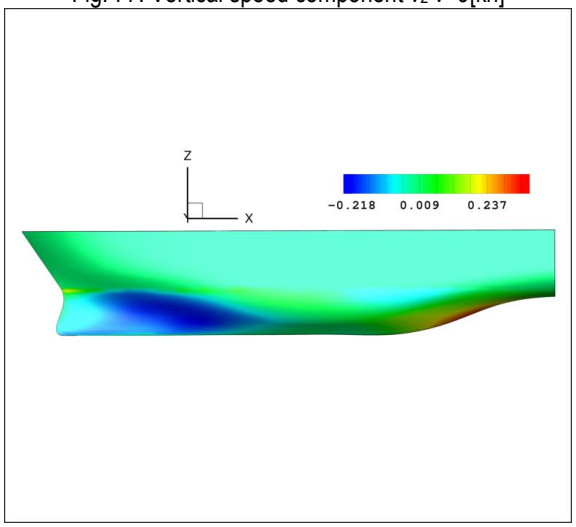

Fig. 79: Vertical speed component v_z v=11[kn]

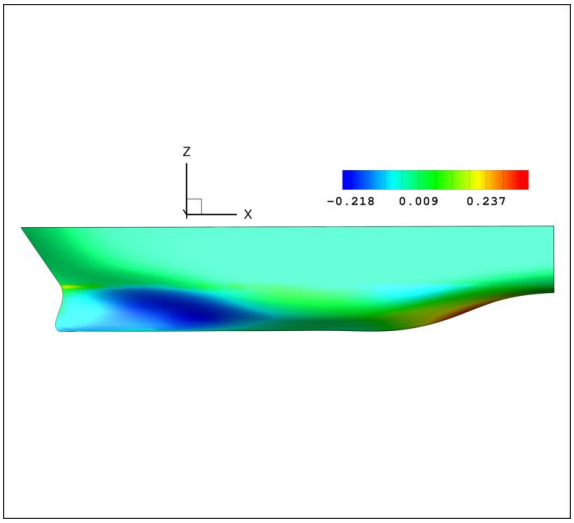

Fig. 80: Vertical speed component v_z v=12[kn]

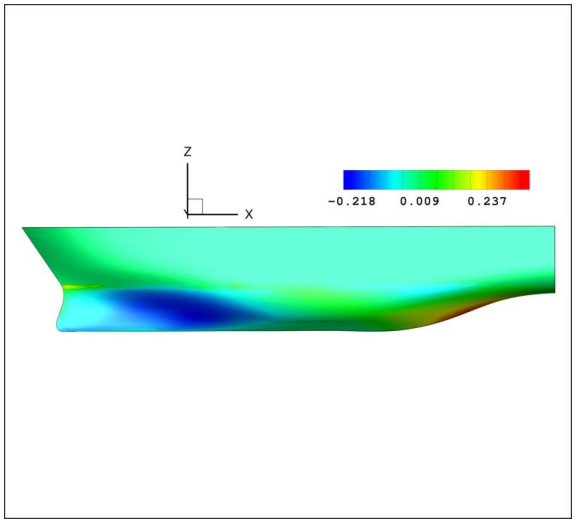

Fig. 81: Vertical speed component v_z v=13[kn]

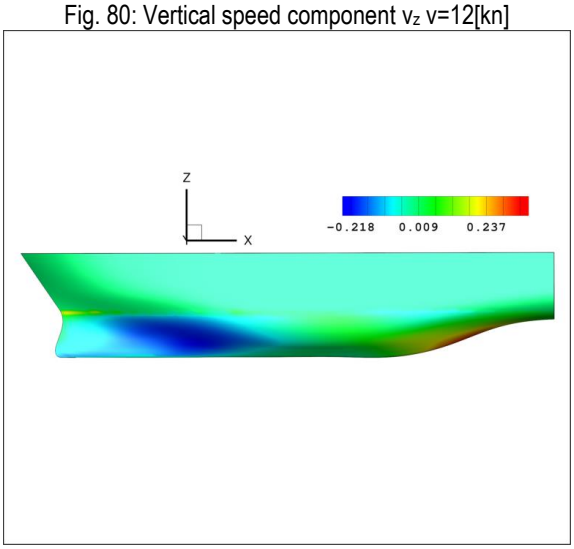

Fig. 82: Vertical speed component v_z v=14[kn]

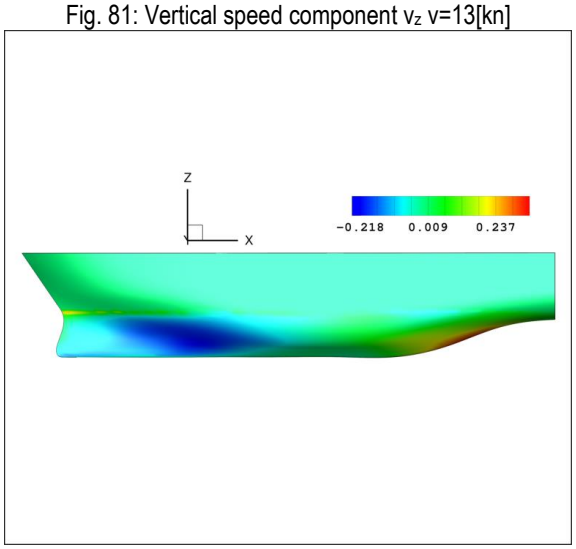

Fig. 83: Vertical speed component v_z v=15[kn]

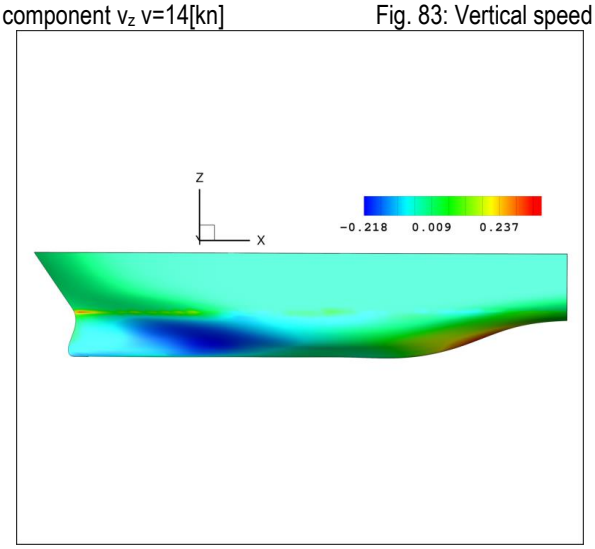

Fig. 84: Vertical speed component v_z v=16[kn]

4.2 Seakeeping predictions

The seakeeping performance sensitivity to the grid is shown in this section. Heave and pitch amplitude RAOs, for the three grids, are compared for 8[kn]≤v≤16[kn], considering incoming head waves and sea state 6, respectively in Figs. 85-93 and Figs. 94-102. The solution changes are small and the results are grid convergent.

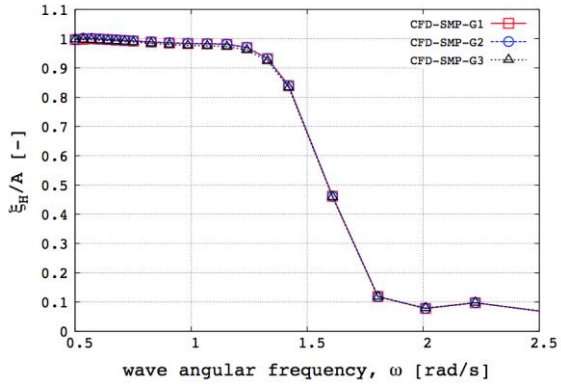

Fig. 85: RAO - heave amplitude v=8[kn]

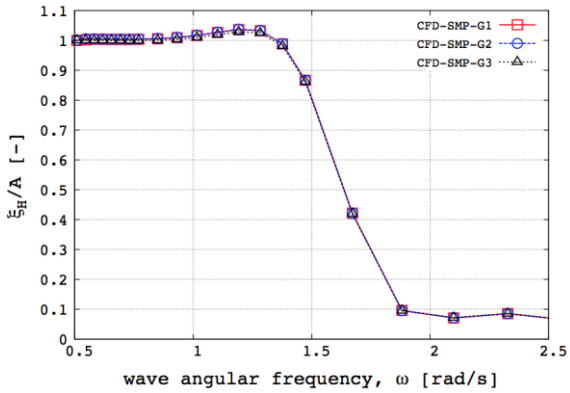

Fig. 86: RAO - heave amplitude v=9[kn]

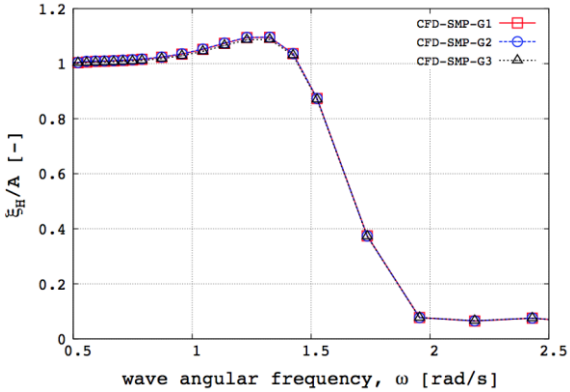

Fig. 87: RAO - heave amplitude v=10[kn]

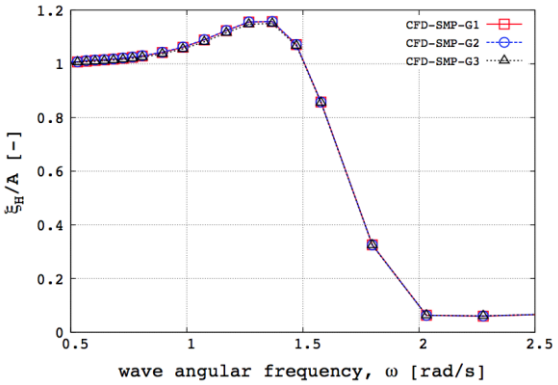

Fig. 88: RAO - heave amplitude v=11[kn]

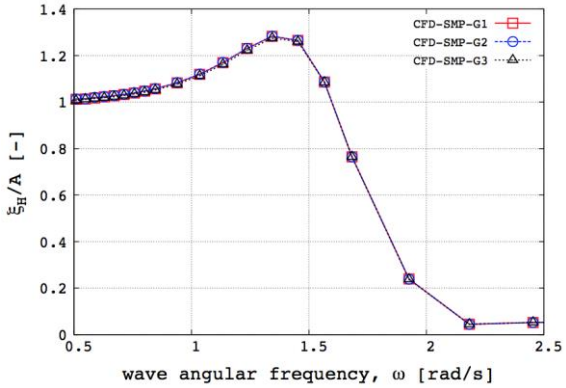

Fig. 89: RAO - heave amplitude v=12[kn]

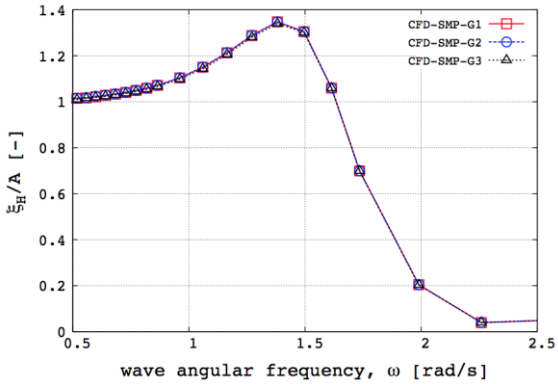

Fig. 90: RAO - heave amplitude v=13[kn]

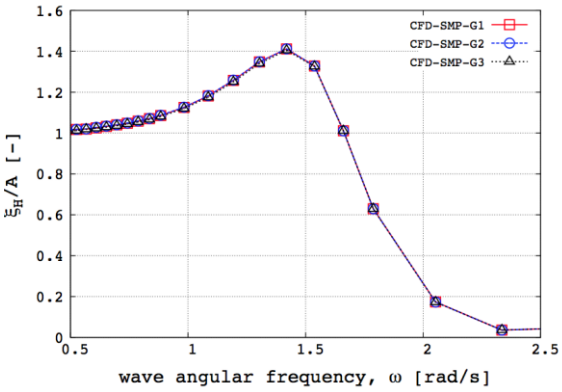

Fig. 91: RAO - heave amplitude v=14[kn]

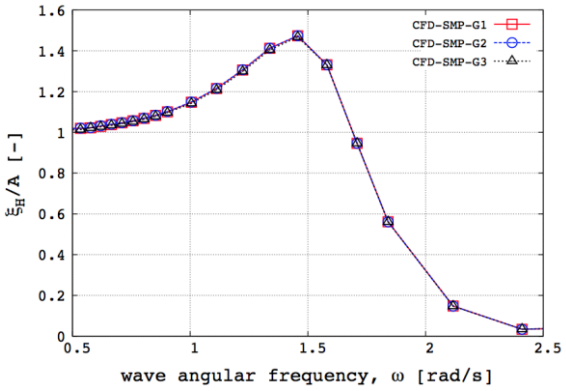

Fig. 92: RAO - heave amplitude v=15[kn]

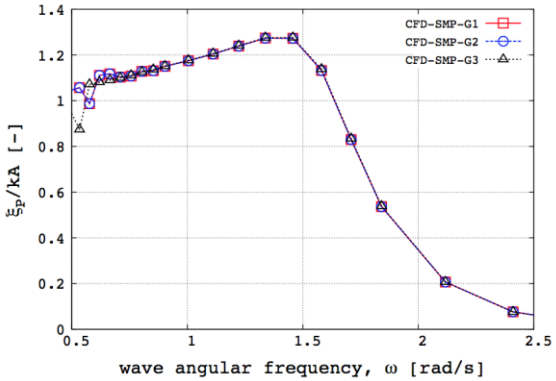

Fig. 93: RAO - heave amplitude v=16[kn]

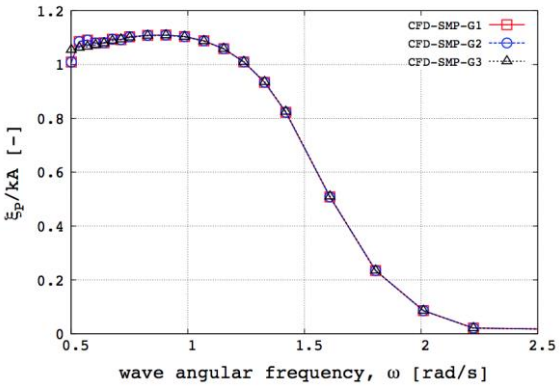

Fig. 94: RAO - pitch amplitude v=8[kn]

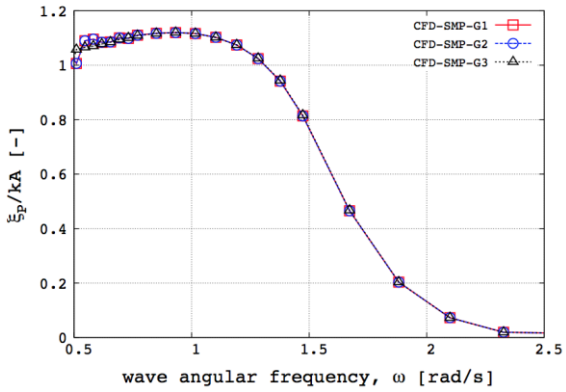

Fig. 95: RAO - pitch amplitude v=9[kn]

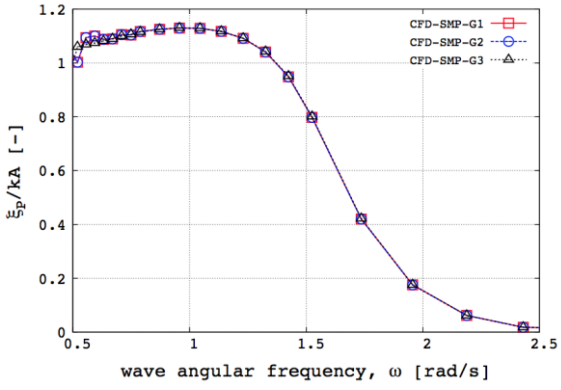

Fig. 96: RAO - pitch amplitude v=10[kn]

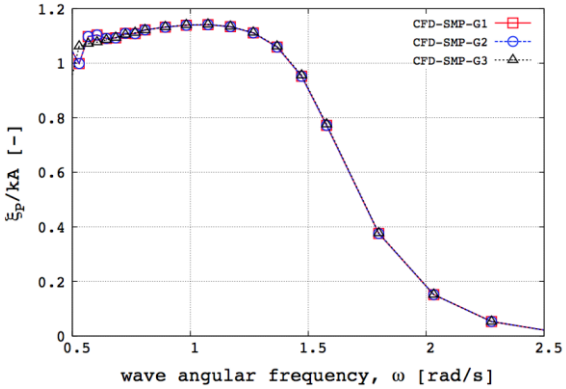

Fig. 97: RAO - pitch amplitude v=11[kn]

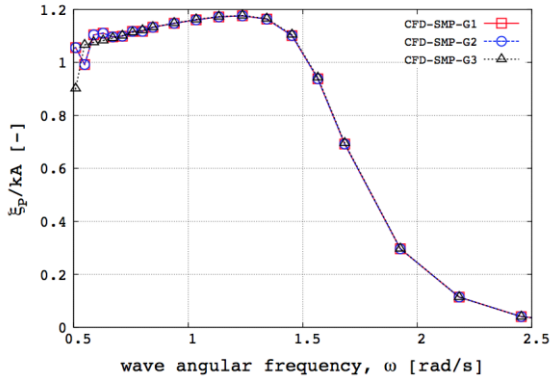

Fig. 98: RAO - pitch amplitude v=12[kn]

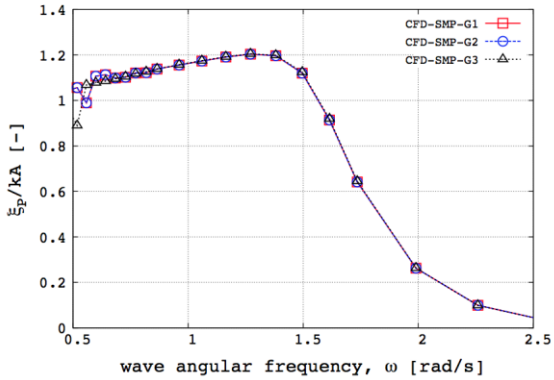

Fig. 99: RAO - pitch amplitude v=13[kn]

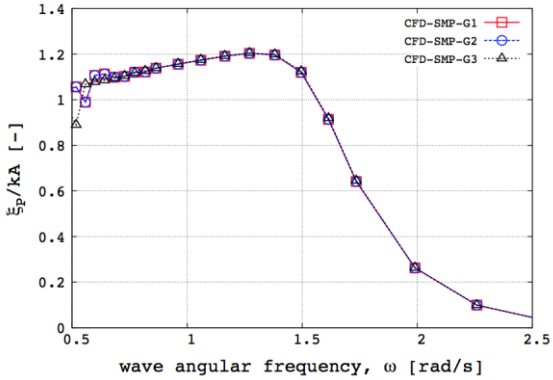

Fig. 100: RAO - pitch amplitude v=14[kn]

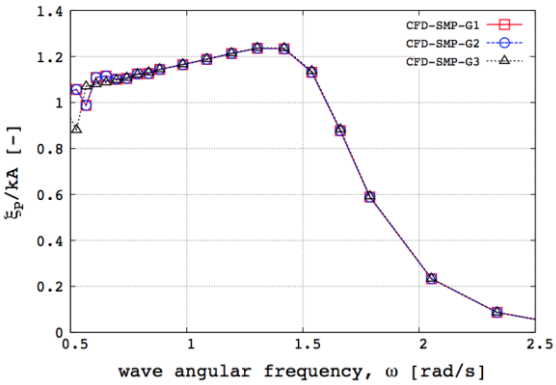

Fig. 101: RAO - pitch amplitude v=15[kn]

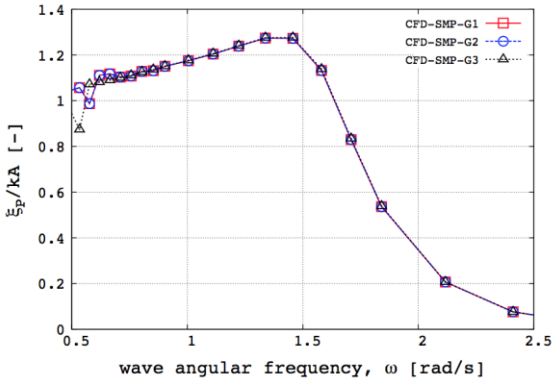

Fig. 102: RAO - pitch amplitude v=16[kn]

4.3 Definition of geometry modifications and design variables

Four orthogonal basis functions and associated design variables are used to modify the hull shape, as summarized in Tab. 8 (see for reference Eqs. (1) and (2)).

The design space is investigated using:

1. two patches (see Tab. 8, j=1;3), which are characterized by a first order function over the entire hull. The shape modification consists in moving volume back/front (Fig. 103(a)) and down/up (Fig. 103(c));
2. two additional patches (see Tab. 8, j=2;4), which introduce a higher-order representation of the hull modifications. Volume is moved back/front (Fig. 103(b)) and down/up (Fig. 103(d)).

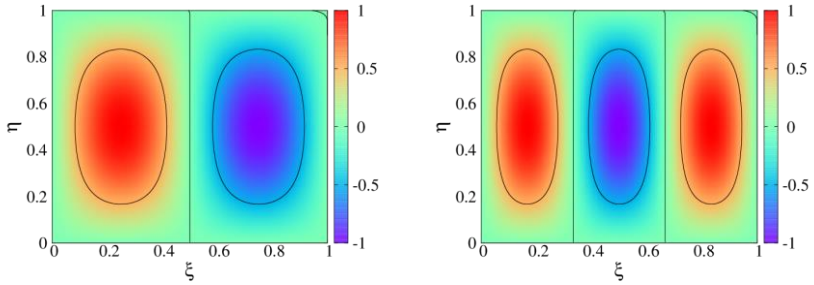

(a) ***(j=1, k=2)*** (b) ***(j=2, k=2)***

(c) ***(j=3, k=2)*** (d) ***(j=4, k=2)***

Figure 103: Orthogonal basis function $\psi_j(\xi,\eta)$ for the 4 design variables.

Table 8: Summary of the patches parameters

							Domain	
Description	j	p_j	ϕ_j	q_j	χ_j	k(j)	$\alpha_{j,\min};\alpha_{j,\max}$	$x_{j,\min};x_{j,\max}$
Hull modification	1	2.0	0	1.0	0	2	-0.25; 0.25	-0.5; 0.5
	2	3.0	0	1.0	0	2	-0.25: 0.25	-0.5; 0.5
	3	1.0	0	2.0	0	2	-0.25; 0.25	-0.5; 0.5
	4	1.0	0	3.0	0	2	-0.25: 0.25	-0.5; 0.5

Figures 104-111 show the original hull compared with the modified one. Maximum and minimum variations for each patch are shown.

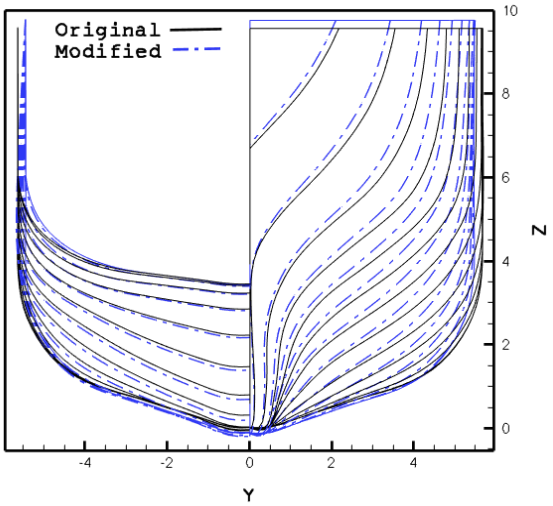

Figure 104: Hull modification with patch 1 - x_{MIN}=-0.5

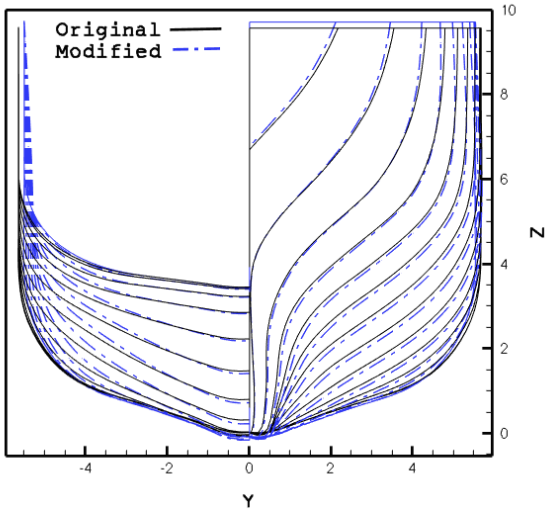

Figure 105: Hull modification with patch 1 – x_{MAX}=0.5

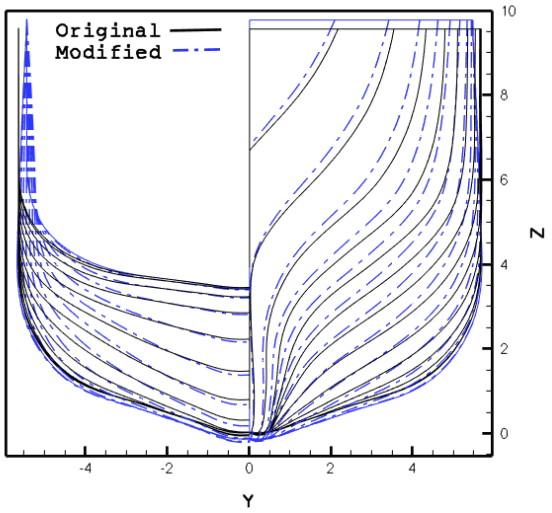

Figure 106: Hull modification with patch 2 - x_{MIN}=-0.5

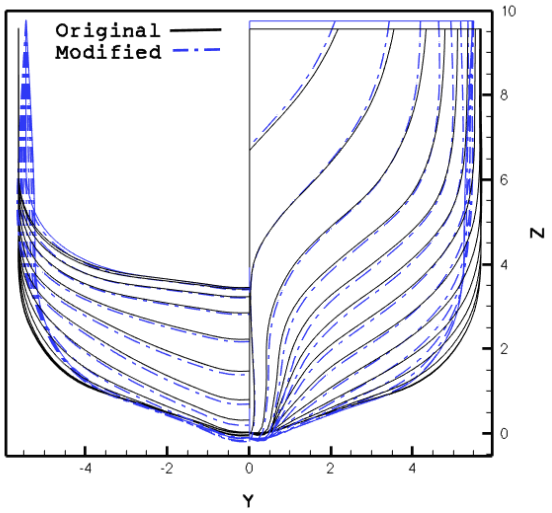

Figure 107: Hull modification with patch 2– x_{MAX}=0.5

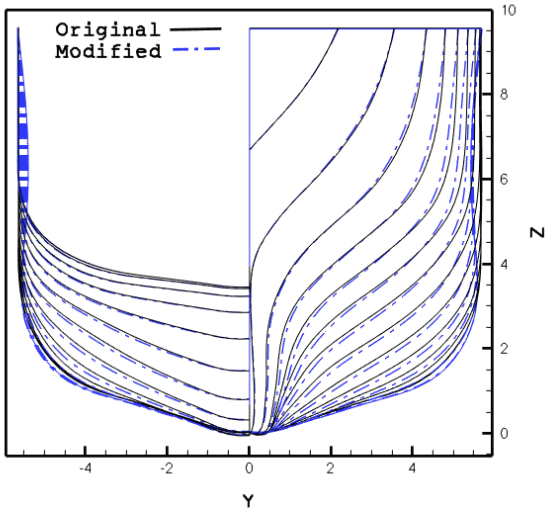

Figure 108: Hull modification with patch 3 - x_{MIN}=-0.5

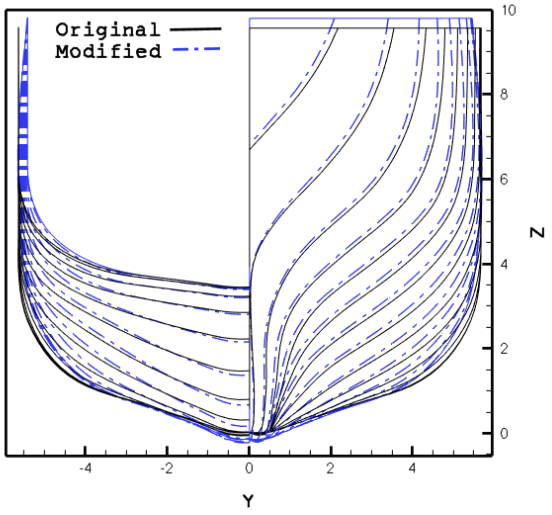

Figure 109: Hull modification with patch 3– x_{MAX}=0.5

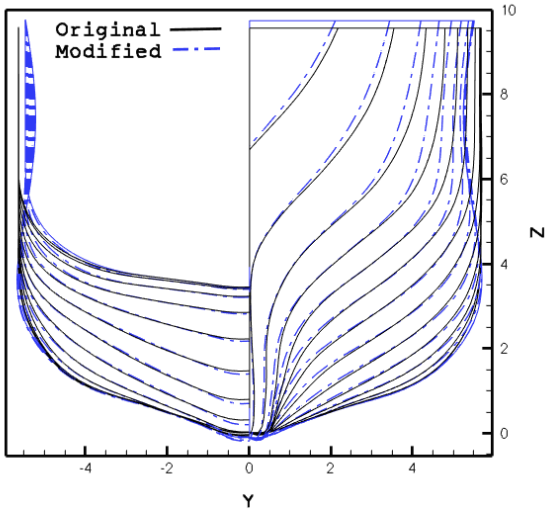

Figure 110: Hull modification with patch 4 - x_{MIN}=-0.5

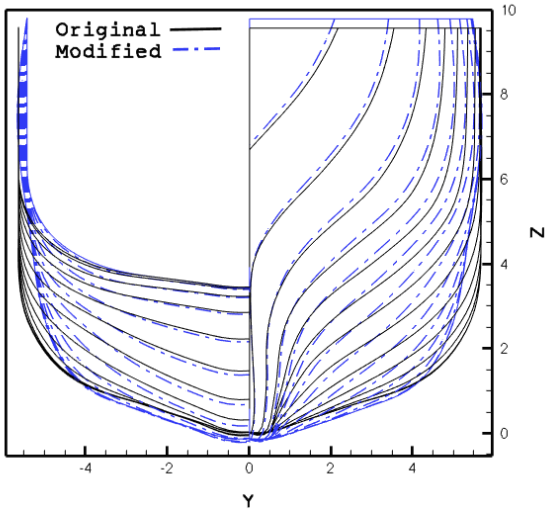

Figure 111: Hull modification with patch 4 – x_{MAX}=0.5

Patches 1 and 2 modify the shape allowing for volume movement from back to front of the hull, patches 3 and 4 control volume modification from up to down.

4.4 Sensitivity analysis to F1

The sensitivity analysis is performed for the overall objective function F1, representing the mean downwards vertical speed component at the bow evaluated in calm water at 12 [kn] (see Fig. 112).

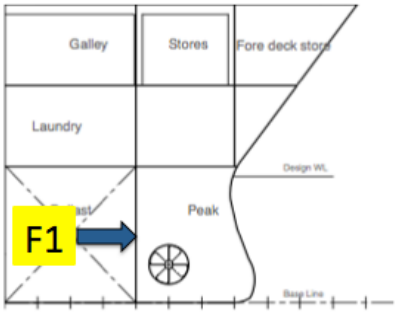

Figure 112: Location of F1 evaluation

Figure 113 shows the independent effects of the hull shapes modifications - defined in order to move volumes aft/forward (x_1,x_2) and down/up (x_3,x_4) on the objective F1. Negative values of ΔF allow for improvements and unfeasible designs are not reported. Specifically, positive values of design variable 1, which means moving volume back to front (using a p=2 order) always result in an increase of performances, whereas positive values of variables 2 and 4, which mean moving volume back to front and up to down (using a p=3 order) lead to a performance decrease. Moving volume up to down using design variable 3 shows conflicting results.

The sensitivity analysis for the F1 shows a possible reduction of the objective function close to 4%.

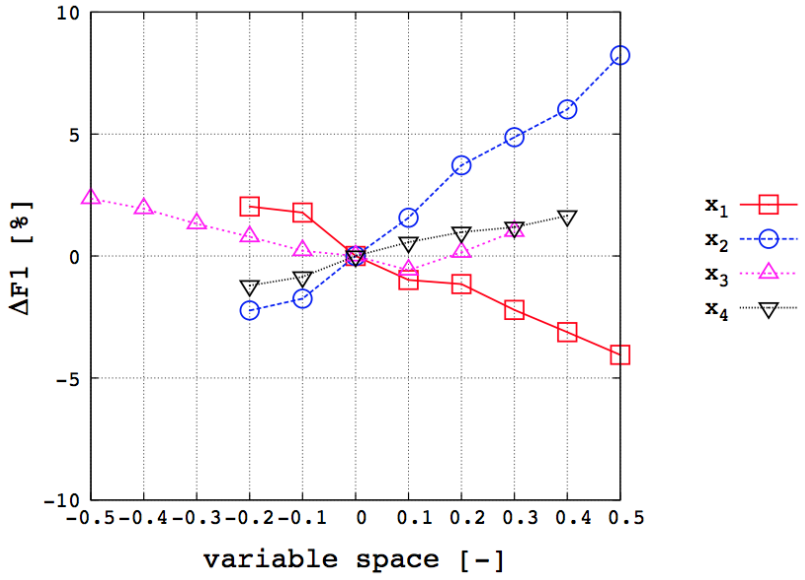

Figure 113: Sensitivity analysis to F1

4.5 Design optimization for F1

Design optimization is performed with

- box constraints defined by $-0.5 \leq x_i \leq 0.5$,
- fixed length and fixed displacement,
- limited variations on beam and draught (+/- 5%).

The optimization reaches a reduction of about the 5% of the objective function F1 as shown in Fig. 114(a). Figure 114(b) presents the values of the corresponding optimal design variables. Figure 115 shows the new hull shape compared to the original.

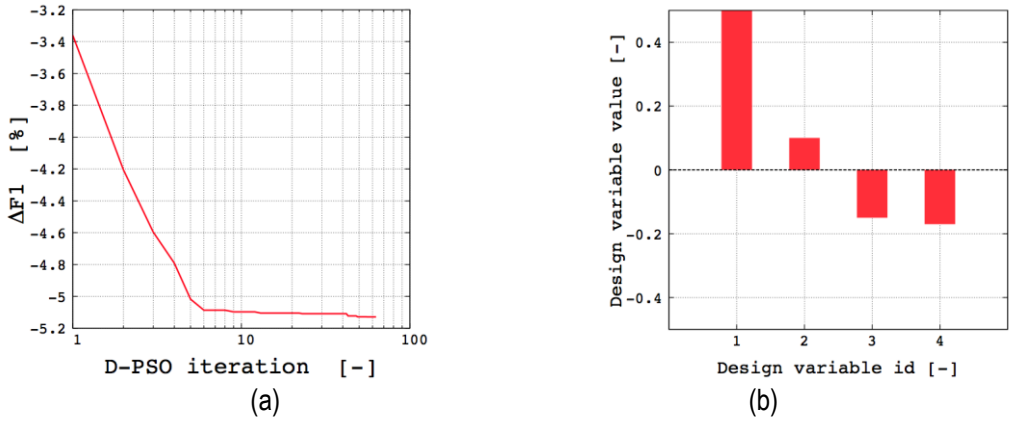

Figure 114: Objective function convergence trend (a) and optimum design variable values (b).

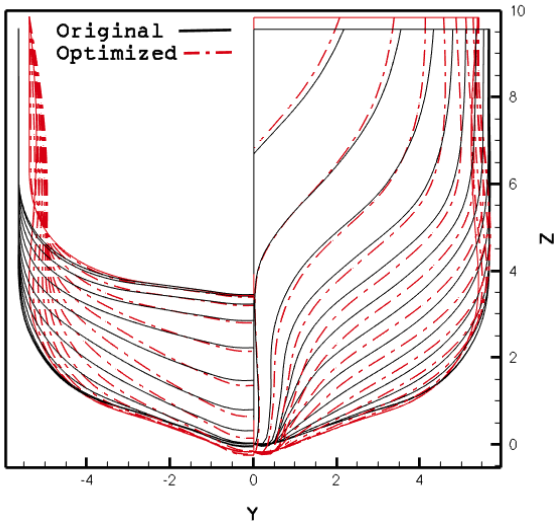

Figure 115: Optimal (red) shape compared to the original (black)

The reduction of the objective function is consistent with the reduction shown in Fig. 116 and 117, where the mean downward vertical component of the speed is presented along with the streamlines on the optimized hull compared to the original.

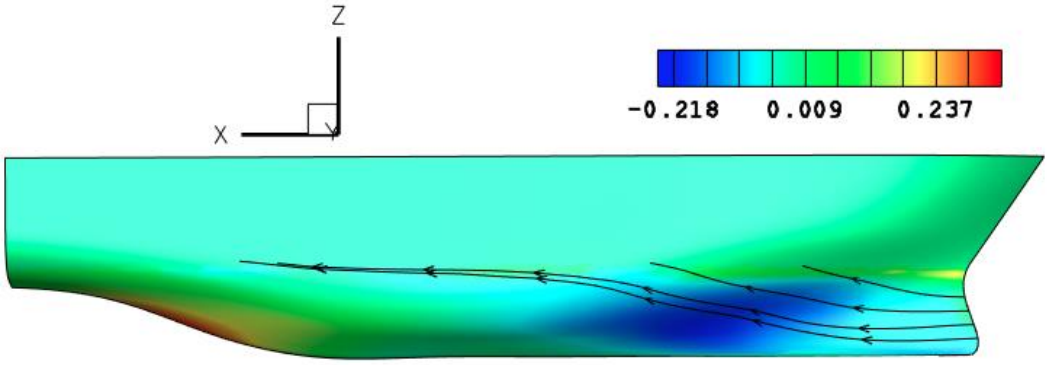

Figure 116: Streamlines trend for the optimized configuration

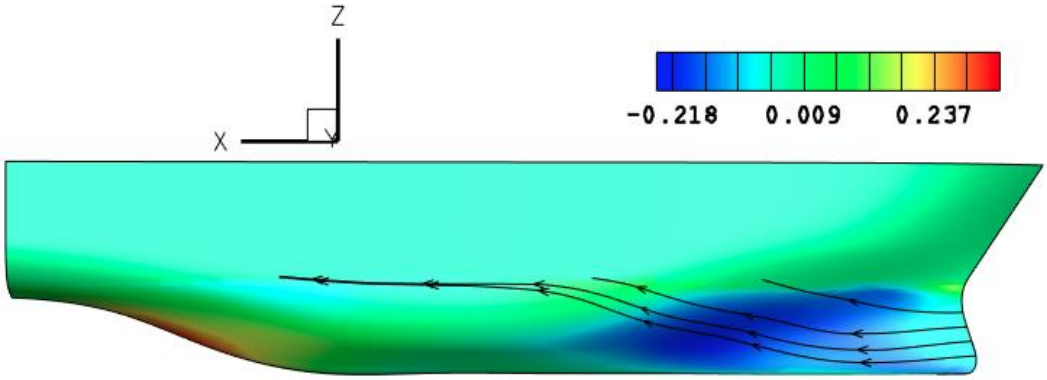

Figure 117: Streamlines trend for the original configuration

4.6 Sensitivity analysis to F2

Seakeeping sensitivity analysis is performed with SMP. The overall objective function F2 that represents RMS of the vertical acceleration at the bow evaluated at sea state 2 and 6 and for v=12[kn], is studied.

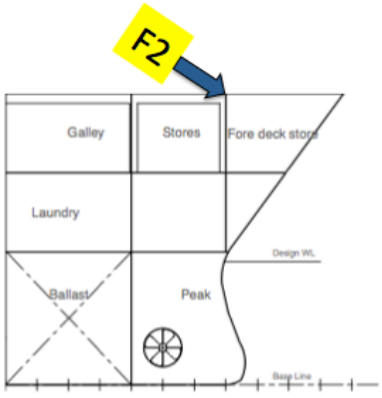

Figure 118: Location of F2 evaluation

Figure shows the sensitivity analysis for the normalized RMS of vertical acceleration of the bow (using a Bretschneider spectrum with a significant wave height equal to 0.3[m] and 5.0[m] and a modal period equal to 3.8[s] and 9.8[s], respectively for sea-state 2 and 6), unfeasible designs are not reported. Specifically, positive values of the whole set of design variables, which means moving volume back to front and up to down, always result in seakeeping performance improvements.

The results show a possible reduction of the objective function close to 8%.

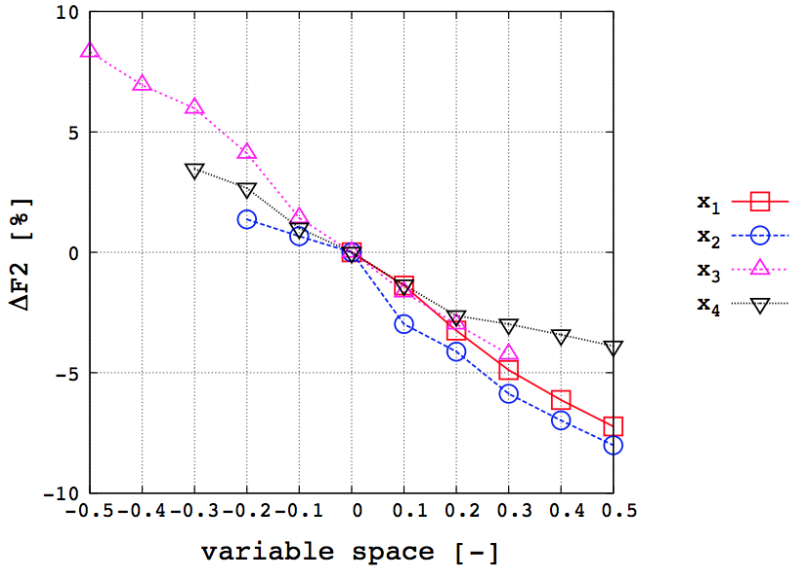

Figure 119: Sensitivity analysis to F2

4.7 Design optimization for F2

Design optimization is performed with

- box constraints defined by $-0.5 \leq x_i \leq 0.5$,
- fixed length between perpendiculars and fixed displacement,
- limited variations on beam and draught (+/- 5%).

The optimization reaches a reduction of about the 9% of the objective function F2 as in Fig. 120(a). Figure 120(b) presents the values of the corresponding optimal design variables, whereas Fig. 121 shows the optimized hull shape compared to the original.

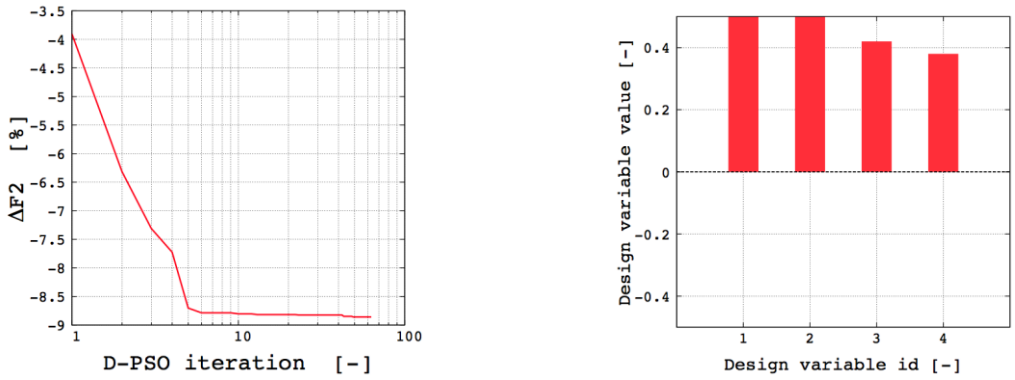

(a) (b)

Figure 120: Objective function convergence trend (a) and optimum design variable (b)

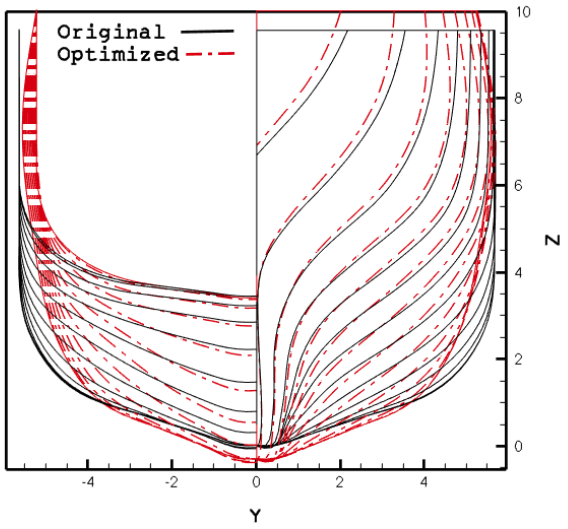

Figure 121: Optimal (red) shape compared to the original (black)

The reduction of the objective function is also consistent with the reduction shown in Fig. 122(a) and (b), where - respectively - the RAOs of heave and pitch for the optimized configuration are compared to the original ones.

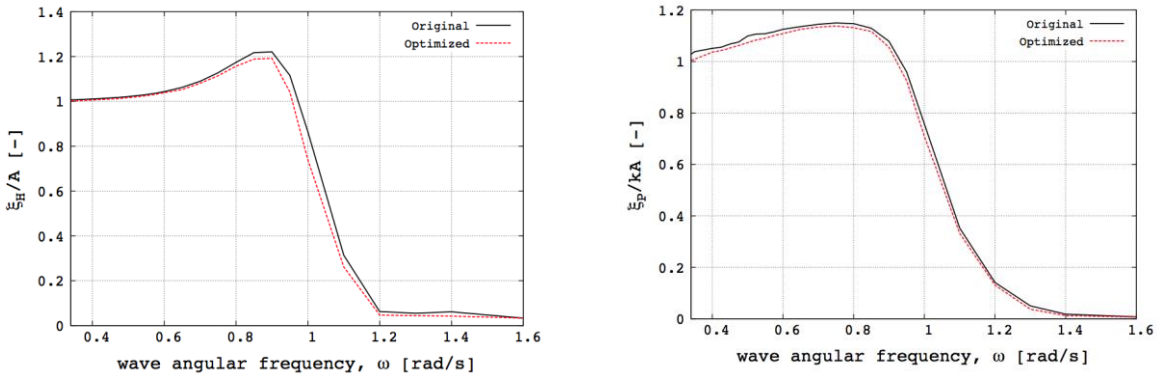

(a) (b)

Figure 122: Optimal shape vs original heave (a) and pitch (b) RAOs

4.8 Multi-objective design optimization

The selection of the optimal hull on the Pareto front (blue point) comes from the best compromise between the two objective functions. Considering the Pareto front achieved, a possible reduction of F1 in between 2 and 5.5% associated with 1.5 to 9% of reduction of F2 considering box constraints defined by $-0.5 \leq x_j \leq 0.5$.

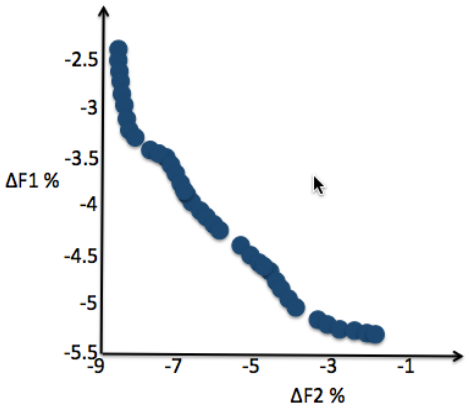

Figure 123: Multi-objective optimization results

5. Bubble sweep down countermeasures: technical devices, suggestions and experimental studies

In this section, indications on technical devices that can be used to mitigate the detrimental effect on measurements of bubble sweep-down are briefly addressed, along with suggestions and an overview of some experimental studies conducted and actually on going on this topic.

Traditionally, gondolas and blisters have been largely used in order to prevent measurements to be affected from bubble sweep-down occurrence. Indeed, they might prevent bubble sweep-down by moving the sonar transducers below the bubbles. Different type of installation can be selected, as shown in Fig. 124.

The gondola can directly lie on the ship hull or can be connected to the ship hull with struts. The latter option might also provide a partial isolation of the transducers from other sources of noise (e.g. the engine noise), although a possible drawback is the extra noise produced from cavitation induced by the struts that can be avoided addressing this issue during their shape design process.

Both the installations, however, imply that the position of the gondola along the hull and its depth should be identified on the basis of preliminary CFD analyses (or towing tank tests) in order to ensure the streamlines – and therefore bubbles - do not impact on the gondola itself (if directly connected to the hull) or lie between the keel and its top surface (if connected with struts).

Figure 124: different installations for gondolas and blisters - sensors are located into a streamlined body outside the hull

Clearly, a deeper submergence of the gondola will ensure higher bubble sweep-down preventing effects. It should be noted that whatever is the installation, the gondola highly increases resistance and, consequently, fuel consumption. Moreover, as the submergence increases, the ship draft and the mount weight also increase, whereas the detection capacity of the transducers (e.g. the multibeam) is reduced.

Besides gondolas, blisters can and have largely been used. The same recommendations provided for gondola in terms of resistance increase, should be however addressed.

It should be also noted that appendices (e.g. bilge keels, flow fence, flow diverting fins, etc.), used to divert streamlines from the transducers area cause a resistance increase. Moreover, especially bilge keels can either generate extra bubbles.

Many vessels are built with a bulbous bow in order to reduce hull resistance and fuel consumption. The problem with a bulb on RVs is that it can result in increased bubble generation when the hull is pitching in waves, and it can also contribute to a water flow pattern around the forward part of the hull that results in an increased amount of bubbles hitting the hydroacoustic antennas installed in the hull, in a gondola and/or in a drop keel.

Many research vessels are therefore designed with a very narrow bow in order to avoid bubble sweep down and also reduce the hull resistance. This is a typical trade off issue when designing a new research vessel, but it can be beneficial to analyze the bubble sweep down effects on an existing vessel and check if a modification to the bulb can result in less bubble sweep down without increasing fuel consumption significantly, or in the best case also reduce hull resistance even more with a new bulb design.

6. Conclusions and recommendations

Indications for design solutions in order to mitigate the bubble sweep-down phenomenon have been derived on the basis of the simulation-based design analyses and optimization. The methodology has been applied to two vessels' hull shapes, with and without bulb. Two objectives pertaining the flow streamlines and the seakeeping performances (essentially heave and pitch) - identified as more relevant when dealing with bubble sweep-down phenomenon – have been addressed.

Specifically, using a multilevel optimization approach the

1) mean downwards velocity component of the flow, which is correlated to the average angle of streamlines, has been evaluated in the bow region of the hull for assigned environmental (sea-state) and operating (speed) conditions;
2) root mean square of the bow vertical acceleration has been evaluated in a prescribed point for assigned environmental (sea-state) and operating condition (speed).

The multilevel optimization approach results can be summarized as follows. According to sensitivity analysis and design optimizations addressing the two objectives separately, the same shape modifications induce different results in terms of local speed at the bow and seekeeping performances. Specifically, moving volume back to front and up to down always result in reducing bow acceleration and heave and pitch motions - both for

hull with and without bulb – and have beneficial effects in mitigating the bubble sweep-down, whereas only back to front volume modifications result in increasing performances in terms of local speed at the bow.

Pertaining to bulbous bow, again results are partially conflicting since narrow bulbs allow for decreasing the local downwards speed component (Figs. 38 and 39 streamlines raised up), whereas enlarged bulbs allow for better seakeeping performances (Figs. 42 and 43).

A trade-off between the two objectives has been achieved performing multi-objective optimization. Following that approach the designer and/or the ship builder and/or the end user can select the hull form on the basis of priorities. If the interest is in enhancing seakeeping performances hull shapes characterized by volume distributions from back to front and up to down and eventually bulb with pretty large width will be chosen, otherwise narrow bulbs should be preferred to enhance performances in terms of local flow at the bow.

Moreover, indications on technical devices that can be used to improve bubble sweep-down performances are addressed. The gondola might prevent bubble sweep-down by moving the sonar transducers below the bubbles. Furthermore, it might also partially isolate the transducers from the noise (e.g. the engine noise). However, it should be underlined that also the depth and the position of the gondola along the hull should be identified on the basis of preliminary CFD analyses (or tank tests) to ensure the streamlines lie between the keel and the top surface of the gondola. As a drawback, it should be noted that the gondola highly increases resistance and, consequently, fuel consumption. Also blisters might be used, addressing the same recommendations provided for the gondola. Bulbous bows, specifically designed to minimize the effect of bubble sweep-down, might be used in order to mitigate the fuel consumption increase. It should be also noted that appendices, such as bilge keels, are potentially a source of bubbles and, as well, cause resistance increase.

As a final indication, the bubble sweep-down phenomenon should be addressed from the early stages of the design process of a RV, including CFD calculations (and eventually tank tests), specifically performed on the configuration under analysis.

7. Acknowledgements

We thank all the WP11 partners for comments that helped in improving this report.

8. References

[1] P. Bassanini, U. Bulgarelli, E.F. Campana, F. Lalli, The wave resistance problem in a boundary integral formulation, *Surv. Math. Ind.* 4: 151-194, 1994.

[2] Telste J.G., Reed A.M., "Calculation of Transom Stern Flows." In Proc. 6th International Conference on Numerical Ship Hydrodynamics, pp. 78-92, 1994.

[3] Schlichting H., Gersten K., Boundary-Layer Theory, Springer-Verlag, Berlin, 2000.

[4] Meyers W.G., Baitis A.E., "SMP84: improvements to capability and prediction accuracy of the standard ship motion program SMP81." DTNSRDC/SPD-0936-04, Sept. 1985.

[5] J. Kennedy and R. Eberhart, "Particle swarm optimization", *Proceedings of the Fourth IEEE Conference on Neural Networks*, Piscataway, NJ, pp. 1942–1948, 1995.

[6] E.F. Campana, G. Liuzzi, S. Lucidi, D. Peri, V. Piccialli, A. Pinto, New global optimization methods for ship design problems, Optim. Eng. 10 (4), pp. 533–555, 2009.

[7] E.F. Campana, M. Diez, U. Iemma, G. Liuzzi, S. Lucidi, F. Rinaldi, A. Serani, Derivative-free global ship design optimization using global/local hybridization of the DIRECT algorithm, Optim. Eng. 17 (1), pp. 127–156, 2015.

[8] A. Serani, C. Leotardi, U. Iemma, E.F. Campana, G. Fasano and M. Diez, "Parameter selection in synchronous and asynchronous deterministic particle swarm optimization for ship hydrodynamics problems", *Applied Soft Computing* Vol. **49**, pp. 313-334, 2016.

[9] Chen X., Diez M., Kandasamy M., Zhang Z., Campana E.F., Stern F., "High-fidelity global optimization of shape design by dimensionality reduction, metamodels and deterministic particle swarm." Engineering Optimization 47(4), pp. 473-494, 2015.

[10] R. Pellegrini, A. Serani, C. Leotardi, U. Iemma, E.F. Campana, M. Diez, "Formulation and parameter selection in multi-objective deterministic particle swarm for simulation-based optimization", in review for *Applied Soft Computing* , 2016.

[11] Trelea I.C., "The particle swarm optimization algorithm: convergence analysis and parameter selection." Information Processing Letters 85, pp. 317-325, 2003.

[12] Wong T.T., Luk W.S., Heng P.A., "Sampling with Hammersley and Halton Points." Journal of Graphics Tools pp. 9-24, 1997.

[13] J. Hotaling, J.M. Meehan, G. Karafiath, "Fisheries Research Vessel Hull and Propeller Design To Maximize Hydroacoustic Survey Efficiency", U.S. Papers for 24th UJNR/MFP, 2001.

[14] G. Karafiath and D.N. McCallum. "Energy efficient hull forms." SNAME Chesapeake Section Meeting, Crystal City VA. December 19, 2000.

[15] Sylvain Delacroix, "Caractérisation de la génération et de la propagation de bulles autour de la carène des navires scientifiques", PhD Thesis 2015, Université de Bretagne Occidentale (DGA/Ifremer).

[16] Bachar MALLAT, "Étude du phénomène d'aération sur les carènes des navires océanographiques, PhD Thesis (in progress), Université Lille Nord de France (Région Haut de France/Ifremer).